NEUROSCIENCE

Astrocytic TDP-43 dysregulation impairs memory by modulating antiviral pathways and interferon-inducible chemokines

Avital Licht-Murava[1,2]*, Samantha M. Meadows[1,2,3], Fernando Palaguachi[1,2], Soomin C. Song[4], Stephanie Jackvony[1,2,3], Yaron Bram[5], Constance Zhou[1,2,6], Robert E. Schwartz[5], Robert C. Froemke[4], Adam L. Orr[1,2]*, Anna G. Orr[1,2,3,6]*

Transactivating response region DNA binding protein 43 (TDP-43) pathology is prevalent in dementia, but the cell type–specific effects of TDP-43 pathology are not clear, and therapeutic strategies to alleviate TDP-43–linked cognitive decline are lacking. We found that patients with Alzheimer's disease or frontotemporal dementia have aberrant TDP-43 accumulation in hippocampal astrocytes. In mouse models, induction of widespread or hippocampus-targeted accumulation in astrocytic TDP-43 caused progressive memory loss and localized changes in antiviral gene expression. These changes were cell-autonomous and correlated with impaired astrocytic defense against infectious viruses. Among the changes, astrocytes had elevated levels of interferon-inducible chemokines, and neurons had elevated levels of the corresponding chemokine receptor CXCR3 in presynaptic terminals. CXCR3 stimulation altered presynaptic function and promoted neuronal hyperexcitability, akin to the effects of astrocytic TDP-43 dysregulation, and blockade of CXCR3 reduced this activity. Ablation of CXCR3 also prevented TDP-43–linked memory loss. Thus, astrocytic TDP-43 dysfunction contributes to cognitive impairment through aberrant chemokine-mediated astrocytic-neuronal interactions.

INTRODUCTION

Subcellular mislocalization and dysregulation of transactivating response region DNA binding protein 43 (TDP-43) is a key pathological hallmark of frontotemporal dementia (FTD) and amyotrophic lateral sclerosis (ALS) (1–4). TDP-43 dysregulation is also common in Alzheimer's disease (AD) and other neurological disorders with pronounced memory loss (5–8). TDP-43 pathology correlates with cognitive deficits and occurs in up to 50% of AD cases, the majority of hippocampal sclerosis cases, and several other dementias (9–13). Despite the prevalence of TDP-43 pathology in various disorders, it is not clear how TDP-43 contributes to disease pathogenesis and cognitive impairments.

TDP-43 is a ubiquitously expressed protein and highly enriched in the nucleus. It is known to regulate RNA processing and transport, among other functions (1–4, 14–17). Mislocalization, deficiency, or mutations in TDP-43 can cause pronounced functional deficits and toxicity in animal and cell culture models (18–21), indicating that alterations in TDP-43 are sufficient to cause impairments. Recent studies suggest that dysfunctional TDP-43 in glial cells and neurons can contribute to neurological disease (6, 9, 22–28). In mice, selective elimination of mutant TDP-43 from motor neurons delays disease onset but does not affect disease progression, implicating mutant TDP-43 in non-neuronal cells as a contributor to chronic pathology (29). Astrocyte-targeted expression of TDP-43^{M337V}, an ALS-associated mutant form of TDP-43, or astrocyte-targeted knockout (KO) of TDP-43 can cause motor deficits (30, 31). In Drosophila, glia-targeted knockdown of a TDP-43 homolog also causes motor deficits (32). In addition, human-induced pluripotent stem cell–derived astrocytes from patients with ALS have cell-autonomous TDP-43 accumulation in the cytoplasm (33). However, the effects of astrocytic TDP-43 alterations on neurocognitive processes, astrocytic-neuronal interactions, and neuronal activities are not known, and therapeutic targets to alleviate cognitive decline in TDP-43–associated disorders have not been defined.

Here, we investigated whether astrocytic TDP-43 is altered in the human brain and how these alterations influence brain function. We found that TDP-43 accumulates in the cytoplasmic compartment of astrocytes in AD and FTD. In mice, induction of analogous TDP-43 alterations in astrocytes throughout the brain or specifically in the hippocampus caused progressive memory loss that correlated with aberrant changes in antiviral factors expressed by hippocampal astrocytes. In particular, cytoplasmic TDP-43 accumulation increased astrocytic levels of interferon (IFN)–inducible chemokines and presynaptic levels of the corresponding chemokine receptor CXCR3, which promoted neuronal hyperexcitability and memory loss. Thus, dementia-associated TDP-43 alterations in hippocampal astrocytes may contribute to cognitive decline through aberrant engagement of antiviral mechanisms and increases in astrocytic-neuronal chemokine signaling.

[1]Appel Alzheimer's Disease Research Institute, Weill Cornell Medicine, New York, NY, USA. [2]Feil Family Brain and Mind Research Institute, Weill Cornell Medicine, New York, NY, USA. [3]Neuroscience Graduate Program, Weill Cornell Medicine, New York, NY, USA. [4]Skirball Institute, Neuroscience Institute, Department of Otolaryngology, New York University Grossman School of Medicine, New York, NY, USA. [5]Department of Medicine, Division of Gastroenterology and Hepatology, Weill Cornell Medicine, New York, NY, USA. [6]Weill Cornell Medicine–Rockefeller–Sloan Kettering Tri-Institutional MD-PhD Program, New York, NY USA.
*Corresponding author. Email: ago2002@med.cornell.edu (A.G.O.); alo2012@med.cornell.edu (A.L.O.); talilicht@gmail.com (A.L.-M.)

RESULTS

Astrocytes have extranuclear TDP-43 accumulation in AD and FTD

Neuronal TDP-43 accumulation in the cytoplasm and other alterations have been well characterized in human samples and model systems. However, TDP-43 pathology is not limited to neurons and might also occur in glial cells, including astrocytes (28, 34). Astrocytes have crucial roles in brain function and can contribute to disease-related changes, such as memory loss, synaptic deficits, and neuroinflammation (35–37). Despite robust endogenous expression of TDP-43 in astrocytes, it is not clear whether astrocytic TDP-43 is altered in patients with dementia-related memory loss and other neurocognitive impairments. Thus, we first assessed subcellular levels of TDP-43 in astrocytes from AD, FTD, and control (nondementia) cases by performing quantitative immunofluorescent labeling for TDP-43 and the astrocyte marker glial fibrillary acidic protein (GFAP) in postmortem human hippocampal sections. Unlike labeling for other prevalent astrocytic markers, labeling for GFAP is sparser and allows for the identification of discrete cells for detailed single-cell neuropathological analyses. Specifically, we measured the levels of TDP-43 immunoreactivity within individual GFAP-positive astrocytic cell bodies and within 4′,6-diamidino-2-phenylindole (DAPI)–positive nuclei of individual astrocytes. Astrocytes were defined by clear GFAP immunolabeling and characteristic cell morphology. In total, over 800 hippocampal astrocytes were analyzed across groups (tables S1 and S2). These single-cell subcellular analyses revealed increased levels of diffuse extranuclear TDP-43 immunoreactivity in hippocampal astrocytes from AD cases as compared to age-matched control cases (Fig. 1, A and B). In contrast, the levels of nuclear TDP-43 immunoreactivity in astrocytes were similar between groups (Fig. 1C). Most notably, the ratio of extranuclear-to-nuclear TDP-43 immunoreactivity in astrocytes was increased by approximately 89% in AD cases as compared to controls (Fig. 1D). Similar alterations in diffuse astrocytic TDP-43 were also detected in the hippocampus of cases with sporadic or familial FTD (Fig. 1, B to D), demonstrating that these effects are not unique to AD and are shared among different disorders. It is possible that similar changes in astrocytic TDP-43 accumulation may also occur in other brain regions and other neurological conditions that affect astrocytes.

Astrocytic TDP-43 alterations cause progressive memory loss

To test whether astrocytic TDP-43 affects behavior and cognitive processes, we generated double transgenic mice with inducible and astrocyte-targeted expression of a mutant form of human TDP-43 that accumulates in the cytoplasm (18). Specifically, we used the well-validated transgenic hGFAP–tetracycline transactivator (tTA) driver line (38–41) to selectively target astrocytes with an inducible tetO-regulated expression of hTDP-43 that contained a mutated nuclear localization sequence (hTDP-43–ΔNLS) (Fig. 2A) (18). This tet-off system enables suppression of hTDP-43–ΔNLS transgene expression using doxycycline (DOX) treatment (39, 40, 42). To prevent potential neurodevelopmental effects, breeding pairs and offspring were maintained on a DOX-supplemented diet until weaning at 3 weeks of age, as described previously (39, 41). By 3 months of age, widespread astrocytic hTDP-43–ΔNLS expression and cytoplasmic accumulation were detected

throughout the brain, including the neocortex, hippocampus, thalamus, striatum, and spinal cord in double transgenic mice, but not in single transgenic or nontransgenic (NTG) controls (Fig. 2, B to D, and fig. S1). Expression of hTDP-43–ΔNLS was robust in astrocytes, which showed characteristic branching and intermingling with neurons, but was minimal or undetectable in neurons (NeuN-positive cells) and microglia/macrophages (Iba1-positive cells) (Fig. 2, B to D, and fig. S1).

Previous studies have reported that targeting hTDP-43–ΔNLS to neurons causes severe motor deficits and early mortality in mice (18) and that an ALS-linked mutant form of hTDP-43 (M337V) expressed in astrocytes is similarly detrimental (30). However, we found that targeting hTDP-43–ΔNLS to astrocytes did not affect lifespan or alter motor, exploratory, and anxiety-linked behaviors (fig. S2). The mice were monitored up to the age of 23 to 24 months and had normal nesting, burying, and social behaviors but had mildly increased grooming by 14 to 15 months of age and increased incidence of ulcerative dermatitis (fig. S2). These results highlight the cell type–specific and mutation-specific effects of TDP-43 on brain function and suggest that cytoplasmic TDP-43 accumulation in astrocytes, in contrast to neurons, is not sufficient to cause early mortality, motor deficits, or changes in other innate behaviors.

TDP-43 pathology frequently occurs in patients with AD or hippocampal sclerosis (5, 9–12, 43) and correlates with memory impairments (10, 44, 45), implicating TDP-43 alterations in memory loss. To determine whether astrocytic hTDP-43–ΔNLS impairs hippocampus-dependent learning and memory, we tested the mice in the Morris water maze. In this task, mice learn to locate a hidden platform using spatial cues (46). One and 3 days after the training was completed, mice underwent memory testing (probe trials) in which the platform was removed and each trained mouse was placed back into the maze for 60 s. Preferences for the target quadrant and the platform location used in training were assessed as compared to other quadrants and analogous nontarget locations in the maze. Mice with intact memory typically have significant preferences for the target quadrant and platform location, whereas mice with diminished memory have no significant preferences for the target quadrant and platform location as compared to other nontarget locations of the maze.

At 3 to 4 months of age, double transgenic ΔNLS mice had normal learning during training and normal memory in a probe test conducted 1 day after training (Fig. 2, E and F). However, the mice were moderately impaired in a probe test conducted 3 days after training (Fig. 2, G and H). By 9 to 10 months of age, double transgenic ΔNLS mice had severely impaired performance in probe tests conducted 1 day and 3 days after training (Fig. 2, J to N) but had no deficits in learning or swimming (Fig. 2I and fig. S3, A and B). By 12 months of age, ΔNLS mice also had deficits in novel object recognition, an alternative memory-dependent test, but no changes in total exploration (Fig. 2O and fig. S3, C and D). Thus, astrocytic hTDP-43–ΔNLS causes progressive memory deficits but does not markedly impair locomotion or other behavioral functions.

Astrocytic TDP-43 alterations in the hippocampus are sufficient to cause memory loss

We next examined whether the memory deficits induced by astrocytic hTDP-43–ΔNLS could be caused by direct effects of astrocytic TDP-43 on the hippocampus, a brain region known to be crucial for
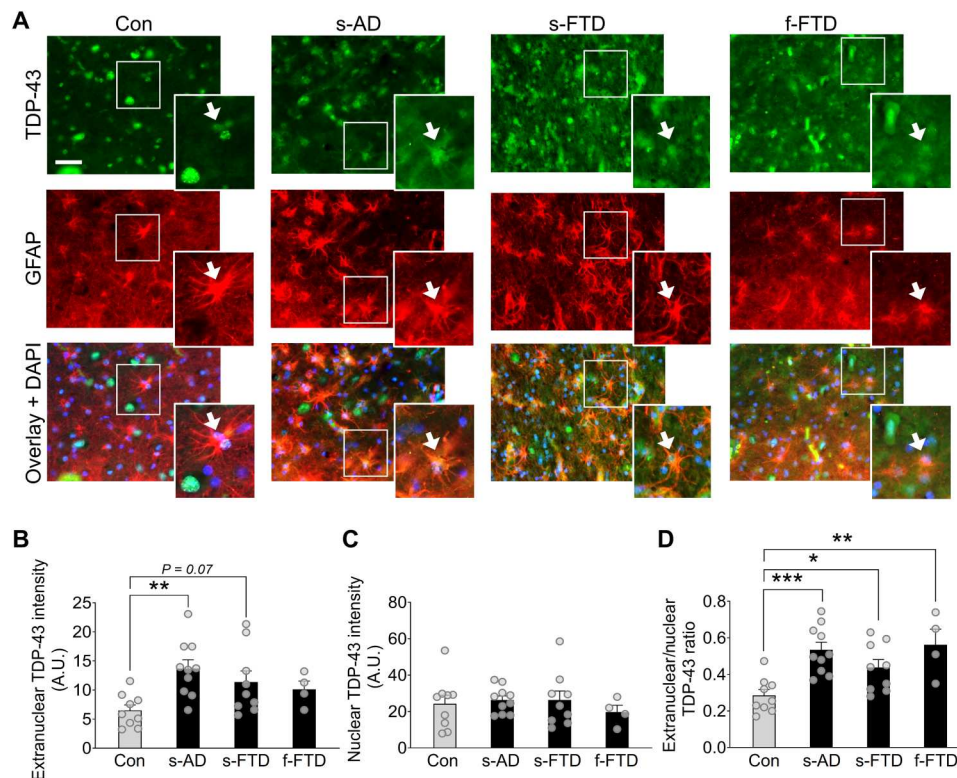
Fig. 1. Human astrocytes have increased extranuclear TDP-43 accumulation in AD and FTD. (**A**) Representative images of TDP-43 immunoreactivity (green) in human postmortem hippocampal sections from nondementia controls (Con), sporadic AD (s-AD), sporadic FTD–TDP-43 (s-FTD), or familial FTD–TDP-43 (f-FTD) cases. The astrocyte marker GFAP (red) was used to visualize astrocytic cell bodies and main processes, and DAPI (blue) was used to visualize cell nuclei within individual astrocytes. Scale bar, 50 μm. (**B** to **D**) Quantification of TDP-43 immunoreactivity within different astrocytic subcellular regions. A.U., arbitrary units. One-way analysis of variance (ANOVA): $F_{(3,28)} = 4.21$, $P = 0.014$ (B); $F_{(3,28)} = 0.34$, $P = 0.80$ (C); and $F_{(3,28)} = 7.56$, $P = 0.0007$ (D); Dunnett's post hoc test: $*P < 0.05$, $**P < 0.01$, and $***P < 0.001$ versus controls.

memory and susceptible to aging and dementia-associated pathology. To selectively target hippocampal astrocytes in vivo, we stereotaxically microinjected adeno-associated viral (AAV) vectors encoding Cre-dependent hTDP-43–ΔNLS or hTDP-43–wild-type (WT) into the hippocampus of transgenic *Aldh1l1*-Cre mice, which express Cre recombinase predominantly in astrocytes (Fig. 3A) (*47*). Although the *Aldh1l1* promoter might be active in other cell types in some contexts and niches of the brain (*48*), recent studies using single-cell transcriptomics and immunolabeling indicate that *Aldh1l1* activity is very low or absent in hippocampal stem cells, including radial glia (*49*, *50*). Moreover, *Aldh1l1* promoter–regulated transgene expression is not detected in neuronal progeny (*50*). Nonetheless, to further restrict transgene expression to astrocytes, we also placed the AAV vector–encoded hTDP-43–ΔNLS and hTDP-43–WT transgenes under the control of the astrocytic promoter *hGfaABC1D* (*51*). This approach created a two-promoter system that requires both *Aldh1l1* and *Gfap* promoter activities for transgene induction. To ensure high efficiency of transgene expression, we used the PHP.eB AAV capsid, which has over 40-fold greater efficiency in transducing neural cells as compared to the standard AAV9 capsid (*52*).

After delivering the vectors intracranially, we performed immunostaining for hTDP-43 protein and markers of astrocytes and other neural cell types. We found that hippocampal transductions with PHP.eB AAV vectors encoding hTDP-43–ΔNLS or hTDP-

43–WT were highly efficient, astrocyte-selective, hippocampus-specific, and stable for months after AAV microinjection (Fig. 3, B to D, and fig. S4, A to C). hTDP-43–ΔNLS was localized in astrocyte cell bodies and processes, whereas hTDP-43–WT was enriched in astrocytic nuclei. However, similar to hTDP-43–ΔNLS, hTDP-43–WT was also moderately extranuclear in vivo and in isolated astrocytes (fig. S4, B, D, and E), as described previously in other cell types (*53*, *54*), suggesting that both manipulations can cause accumulation of TDP-43 in the cytoplasm.

We next used the Morris water maze to assess learning and memory in AAV-injected transgenic *Aldh1l1*-Cre mice and AAV-injected NTG littermate controls. Three months after microinjection, *Aldh1l1*-Cre mice that received AAV vector encoding hTDP-43–ΔNLS had normal learning and probe performance (Fig. 3, E and F). However, by 6 months after microinjection, these mice had impaired probe performance as compared to control groups (Fig. 3, G to I), similar to the results obtained in double transgenic hTDP-43–ΔNLS mice (Fig. 2). NTG mice that received the AAV vector encoding hTDP-43–ΔNLS but did not express Cre performed similarly to control *Aldh1l1*-Cre mice that did not receive the AAV vectors, ruling out nonspecific effects by the AAV vectors. Notably, *Aldh1l1*-Cre mice that received the AAV vector encoding hTDP-43–WT had normal learning but impaired probe performance by 9 months after microinjection (Fig. 3, K to O), consistent with previous studies showing that accumulation of WT

Fig. 2. Astrocytic TDP-43 alterations cause progressive memory loss. (**A**) Schematic of the tet-off transgenic system used to induce astrocytic expression of hTDP-43 containing ΔNLS. E0, embryonic day 0. (**B**) Top rows: hTDP-43 (green) in hippocampal sections from 3-month-old NTG, *hGFAP*-tTA (tTA), and *tetO*–hTDP-43–ΔNLS (tetO) control mice or double transgenic ΔNLS mice. Scale bar, 200 μm. Bottom row: Total TDP-43 (green) and astrocyte marker GFAP (red). DAPI (blue) was used to visualize nuclei. Scale bar, 25 μm. (**C**) hTDP-43 in the hippocampal dentate gyrus (DG) and CA1 regions of ΔNLS mice. Graphs show the percentage of GFAP- or NeuN-immunoreactive cells that were also hTDP-43–positive. (**D**) hTDP-43 (green) in ΔNLS mice; astrocyte marker GFAP (magenta). Insets show magnified views. Scale bar, 300 μm. (**E** to **N**) Morris water maze testing at 3 to 4 (E to H) and 9 to 10 (I to N) months of age. (E) Distance traveled to reach target platform during hidden platform training. Repeated-measures two-way ANOVA: $F_{(6,102)} = 1.141$, $P = 0.344$ for interaction and $F_{(3,51)} = 2.635$, $P = 0.0596$ for genotype. (F to H) Probe trials. Durations in target and nontarget (other) quadrants. One-way ANOVA (target): $F_{(3,49)} = 0.06677$, $P = 0.9773$ (F) and $F_{(3,49)} = 1.882$, $P = 0.1448$ (G). Student's t test with Welch's correction: **$P < 0.01$ and ***$P < 0.001$ versus other. NS, no significant preference. (H) Swim paths during 72-hour probe; insets show magnified views of target. (I) Distance traveled during training. Repeated-measures two-way ANOVA: $F_{(12,263)} = 0.3298$, $P = 0.9834$ for interaction and $F_{(3,66)} = 2.278$, $P = 0.0877$ for genotype. (J to L) Probe trials. One-way ANOVA (target): $F_{(3,66)} = 5.372$, $P = 0.0023$ (J) and $F_{(3,65)} = 3.548$, $P = 0.0192$ (K); Dunnett's test: ##$P < 0.01$ and ###$P < 0.001$ versus NTG target. Student's t test with Welch's correction: *$P < 0.05$, **$P < 0.01$, and ***$P < 0.001$ versus other. (L) Swim paths. (M and N) Probe trials. Student's t test with Welch's correction: *$P < 0.05$, **$P < 0.01$, and ***$P < 0.001$ versus other. (**O**) Novel object recognition (NOR) test. One-way ANOVA and Dunnett's test: *$P < 0.05$ versus NTG.
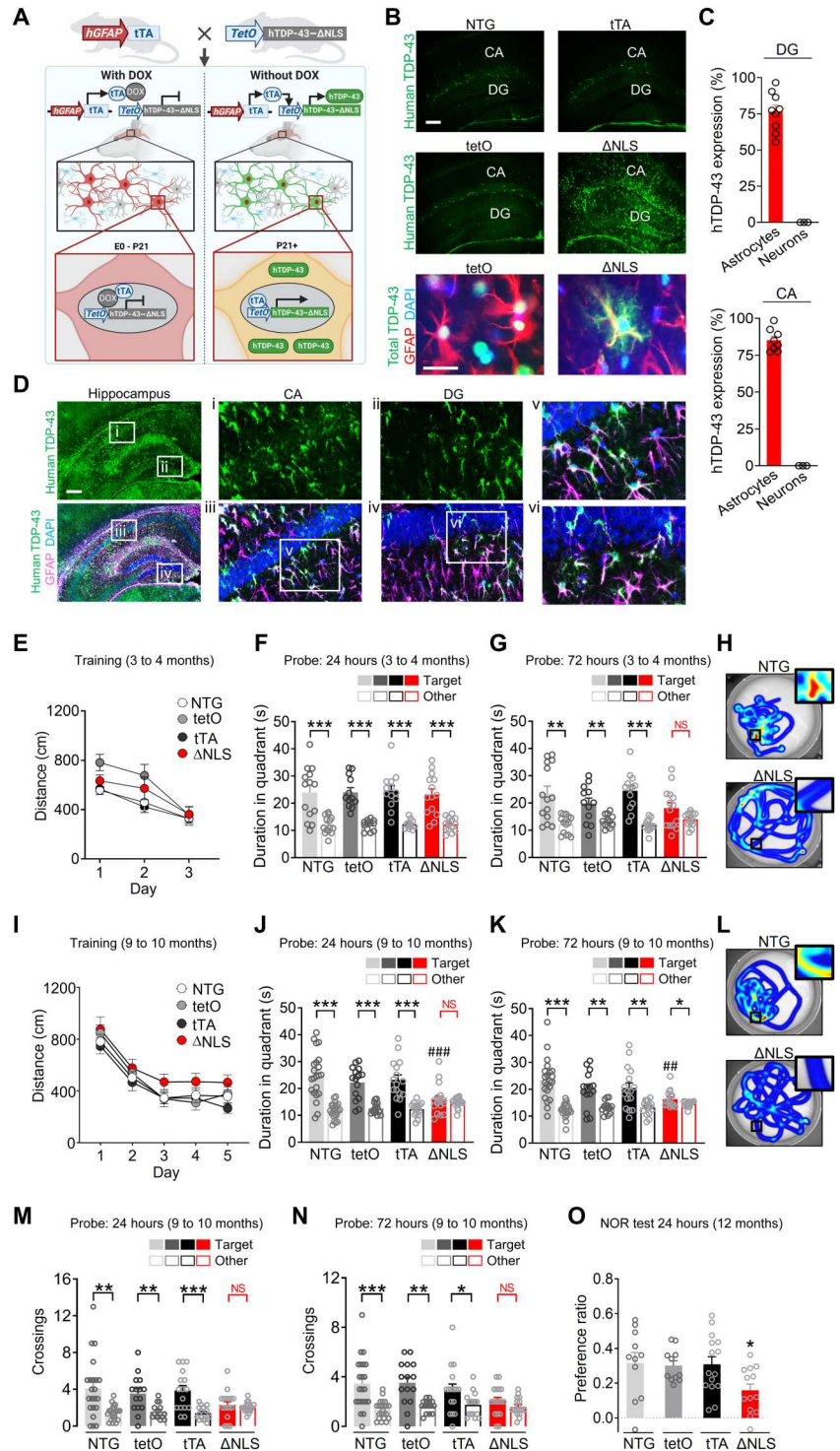
TDP-43 is also detrimental (*53–55*). All groups had similar swim speeds (Fig. 3, J and P).

In addition, using our two-promoter system, we tested whether chronic astrocytic overexpression of other unrelated proteins would similarly cause progressive memory loss. To test this, we transduced hippocampal astrocytes with a PHP.eB AAV vector encoding hM4Di-mCherry (instead of hTDP-43) under the control of the *hGfaABC₁D* promoter. We did not detect memory deficits in *Aldh1l1*-Cre or NTG mice that received this vector (fig. S4, F to K), further ruling out potential nonspecific effects of AAV transduction and protein overexpression. Together, these results suggest that dysregulation of TDP-43 in hippocampal astrocytes is sufficient to cause progressive memory deficits and that TDP-43 plays essential roles in astrocytic modulation of hippocampal function.
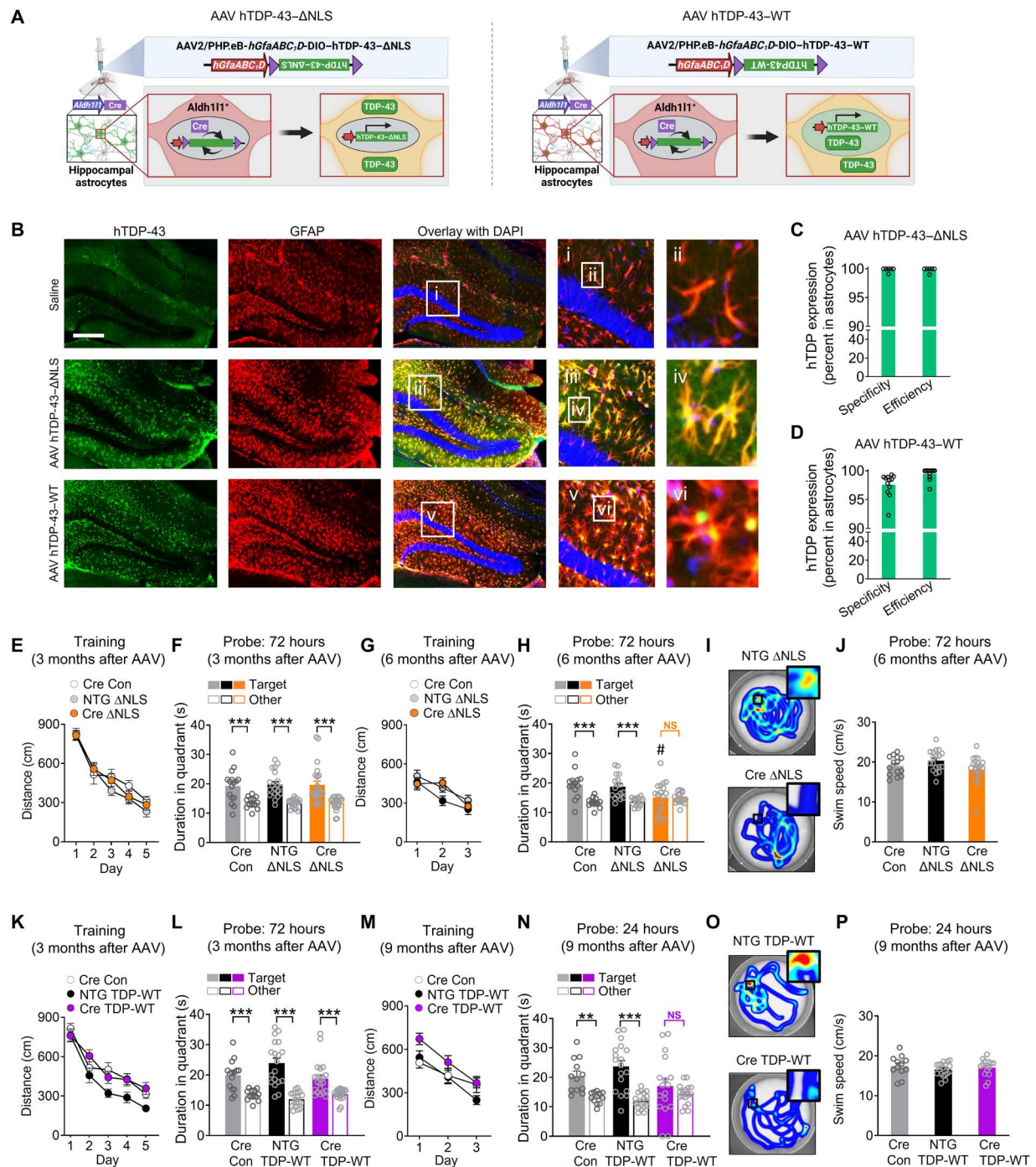
Fig. 3. Hippocampus-targeted astrocytic TDP-43 alterations are sufficient to cause progressive memory loss. (**A**) Schematic of AAV-mediated transgene expression. (**B**) hTDP-43 (green) and astrocytic marker GFAP (red). DAPI (blue) was used to visualize nuclei. Yellow indicates overlay of green and red channels. Insets i to vi show magnified views. Scale bar, 300 μm. (**C** to **D**) hTDP-43 expression. Specificity was defined as a percent of hTDP-43–immunoreactive cells in CA1 and dentate gyrus regions that were also GFAP-positive; efficiency was a percent of GFAP-immunoreactive cells that were also hTDP-43–positive. (**E** to **J**) *Aldh1l1*-Cre (Cre) or NTG mice were injected at 2 to 3 months of age and tested in the Morris water maze at 3 or 6 months after injection. (E and G) Distance traveled during hidden platform training. Repeated-measures two-way ANOVA: (E) $F_{(8,224)} = 0.84$, $P = 0.57$ for interaction and (G) $F_{(4,96)} = 1.17$, $P = 0.33$ for interaction. (F and H) Probe trials. Durations in target and nontarget (other) quadrants. (H) One-way ANOVA (target): $F_{(2,46)} = 4.18$, $P = 0.016$; Dunnett's post hoc test: #$P < 0.05$ versus *Aldh1l1*-Cre/control target. Student's *t* test with Welch's correction: ***$P < 0.001$ versus other. (I) Swim paths during the 72-hour probe; insets show magnified views of the target platform area. (**K** to **P**) *Aldh1l1*-Cre or NTG mice were injected at 2 to 3 months of age and tested in the Morris water maze at 3 or 9 months after injection. (K and M) Distance traveled during training. Repeated-measures two-way ANOVA: (K) $F_{(8,216)} = 0.99$, $P = 0.44$ for interaction and $F_{(2,54)} = 7.19$, $P = 0.0017$ for group; (M) $F_{(4,88)} = 1.06$, $P = 0.38$ for interaction and $F_{(2,44)} = 5.06$, $P = 0.0105$ for group. (L and N) Probe trials. Durations in target and nontarget (other) quadrants. Student's *t* test with Welch's correction: **$P < 0.01$ and ***$P < 0.001$ versus other. (O) Swim paths during the 24-hour probe trial. (J and P) Swim speeds during indicated probe trials.

Astrocytic TDP-43 affects IFN-inducible chemokines and other antiviral factors in a cell-autonomous manner

Astrocytes contribute to memory loss in disease (*39*, *56*, *57*), but the exact mechanisms are not known. In addition, the effects of TDP-43 on astrocytes and astrocytic-neuronal interactions remain unclear. In other cell types, TDP-43 dysfunction can alter inflammatory cascades (*58*, *59*), which might promote cognitive decline. Therefore, we next examined whether double transgenic ΔNLS mice had altered transcription of genes linked to neuroinflammation and glial reactivity in different brain regions that expressed hTDP-43–ΔNLS. Targeted transcriptional profiling was carried out in four different brain regions across four genotypes using a microfluidic-based high-throughput reverse transcription quantitative polymerase chain reaction (RT-qPCR) and a custom-designed panel of curated neuroinflammation-related genes. Tau-P301S mice were used as a technical positive control because this model has robust hippocampal gliosis and neuroimmune responses. In contrast to the broad changes in hippocampal gene expression detected in Tau-P301S mice (*60*, *61*), we found highly selective changes in gene expression in double transgenic ΔNLS mice (Fig. 4A). IFN-inducible chemokines *Cxcl9* and *Cxcl10* were among the top genes affected and were highly increased in the hippocampus but showed minimal changes in other brain regions, including the neocortex, striatum, and thalamus (Fig. 4, A to C, and fig. S5, A to C). Various markers of astrocytic and microglial reactivity were minimally affected at the RNA and protein levels (Fig. 4A and fig. S5, A to C and F). Notably, the increases in CXCL9 and CXCL10 proteins were localized to hippocampal astrocytes, but not neurons, microglia/macrophages, or astrocytes in other examined brain regions (Fig. 4, D and E, and fig. S5, D and E), similar to previous findings in humans with AD (*62*). Increases in astrocytic CXCL9 and CXCL10 protein levels were also detected in transgenic *Aldh1l1*-Cre mice that received intrahippocampal injections of PHP.eB AAV vectors encoding hTDP-43–ΔNLS or hTDP-43–WT (fig. S5G), suggesting that astrocytic induction of these chemokines does not require widespread transgene expression and is not unique to the transgenic tet-off system. In addition to CXCL9 and CXCL10, the related chemokine CXCL11 also binds to CXCR3 with high affinity. However, in C57Bl/6 mice (which were used in this study), CXCL11 is not expressed at the protein level because of a premature stop codon (*63*, *64*).

Increased expression of CXCL9 to CXCL11 is typically induced by antiviral or IFN-associated signaling, which regulates glial functions and is linked to cognitive changes, dementia, and neuropsychiatric disorders (*65–70*). One of the primary triggers for antiviral or IFN-associated signaling is activation of pattern recognition receptors (PRRs) that detect non-self or aberrant nucleic acids. Thus, we next tested whether sensors of nucleic acids were altered in transgenic mice and isolated astrocytes expressing hTDP-43–ΔNLS. Double transgenic mice expressing astrocytic hTDP-43–ΔNLS had increased levels of multiple sensors of aberrant double-stranded RNA (dsRNA), including RIG-I (retinoic acid–inducible gene 1; also known as *Ddx58*), MDA5 (melanoma differentiation–associated gene 5; also known as *Ifih1*), and PKR (dsRNA-dependent protein kinase; also known as *Eif2ak2*) (Fig. 4F). We also detected increased levels of other antiviral factors, including viperin (virus inhibitory protein, endoplasmic reticulum–associated, IFN-inducible; also known as *cig5* or *Rsad2*) and IRF-7 (IFN regulatory factor-7), a master regulator of IFN responses (Fig. 4G). Similar to the

chemokines, the increases in viperin protein levels were localized to astrocytes but not neurons (Fig. 4H and fig. S5H). In contrast to the dsRNA sensors, we did not detect changes in the genes encoding double-stranded DNA (dsDNA) sensor cyclic guanosine 5′-monophosphate–adenosine 5′-monophosphate (AMP) synthase (cGAS) or stimulator of IFN genes (STING) (fig. S5I), suggesting that astrocytic TDP-43 alterations may preferentially affect dsRNA sensors and other alternative dsDNA-sensing mechanisms.

Next, we examined whether the changes in astrocytic gene expression were cell-autonomous and linked to functional changes in immune-related signaling. For these experiments, primary astrocytes were isolated from the hippocampus of double transgenic ΔNLS or NTG control mice generated in breeding cages with standard chow without DOX. Cell culture purity and transgene efficiency and specificity were evaluated as described in Materials and Methods. As expected, isolated ΔNLS but not NTG astrocytes expressed hTDP-43–ΔNLS protein (Fig. 5A). Total TDP-43 levels were less than twofold greater than endogenous TDP-43 levels (Fig. 5, A and B), and TDP-43 aggregates were not detected (see the Supplementary Materials). Nonetheless, isolated ΔNLS astrocytes had increased levels of multiple IFN-related gene transcripts, including dsRNA-related PRRs (Fig. 5C), *Rsad2*/viperin, *Ifnb1*, and *Ifng* (Fig. 5D), suggesting that these gene changes are at least in part cell-autonomous. Isolated ΔNLS astrocytes also had increased levels of XCL10 protein in the lysates and secreted into the medium (Fig. 5, E and F), as well as enhanced levels of IFN-γ in the lysates (Fig. 5G). In addition, isolated ΔNLS astrocytes had increased levels of phosphorylated nuclear factor κB (NF-κB) (Fig. 5, H and I), supporting the notion that TDP-43 dysfunction affects immune-related signaling pathways in astrocytes (*71*), similar to neurons and microglia (*59*, *72*). However, treating astrocytes with SN50, a cell-permeable peptide that inhibits NF-κB nuclear translocation (*73*), did not prevent the increases in *Cxcl10* and *Cxcl9* (Fig. 5, J and K). In contrast, treating astrocytes with Stattic, a potent inhibitor of signal transducer and activator of transcription 3 (STAT3) (*74*), was effective in blocking *Cxcl10* and *Cxcl9* gene expression changes (Fig. 5, J and K).

To further test whether the changes in signaling and chemokine expression were induced by TDP-43–ΔNLS, some ΔNLS and NTG astrocytes isolated from the hippocampus were maintained in DOX-supplemented medium. As expected, DOX-treated ΔNLS astrocytes had minimal expression of hTDP-43, and total TDP-43 levels were reduced by approximately half as compared to ΔNLS astrocytes maintained without DOX (Fig. 5, L and M). DOX-treated ΔNLS astrocytes had reduced levels of *Cxcl10* gene expression (Fig. 5N) and reduced levels of phosphorylated NF-κB and STAT3 (Fig. 5O) as compared to astrocytes maintained without DOX, suggesting that NF-κB and Janus kinase–STAT pathways are both engaged by TDP-43 alterations. These signaling pathways were not affected in NTG control astrocytes treated with DOX. Thus, TDP-43 alterations enhanced astrocytic antiviral gene expression and immune-related signaling and increased chemokine production.

Although the approximately twofold increases in total levels of TDP-43 induced moderate changes in gene expression and signaling, these changes were chronic and associated with marked functional effects on antiviral responses to pathogens. To examine these effects, we used a mimic of viral dsRNA, polyinosinic-polycytidylic acid [poly(I:C)], as a positive control for induction of antiviral
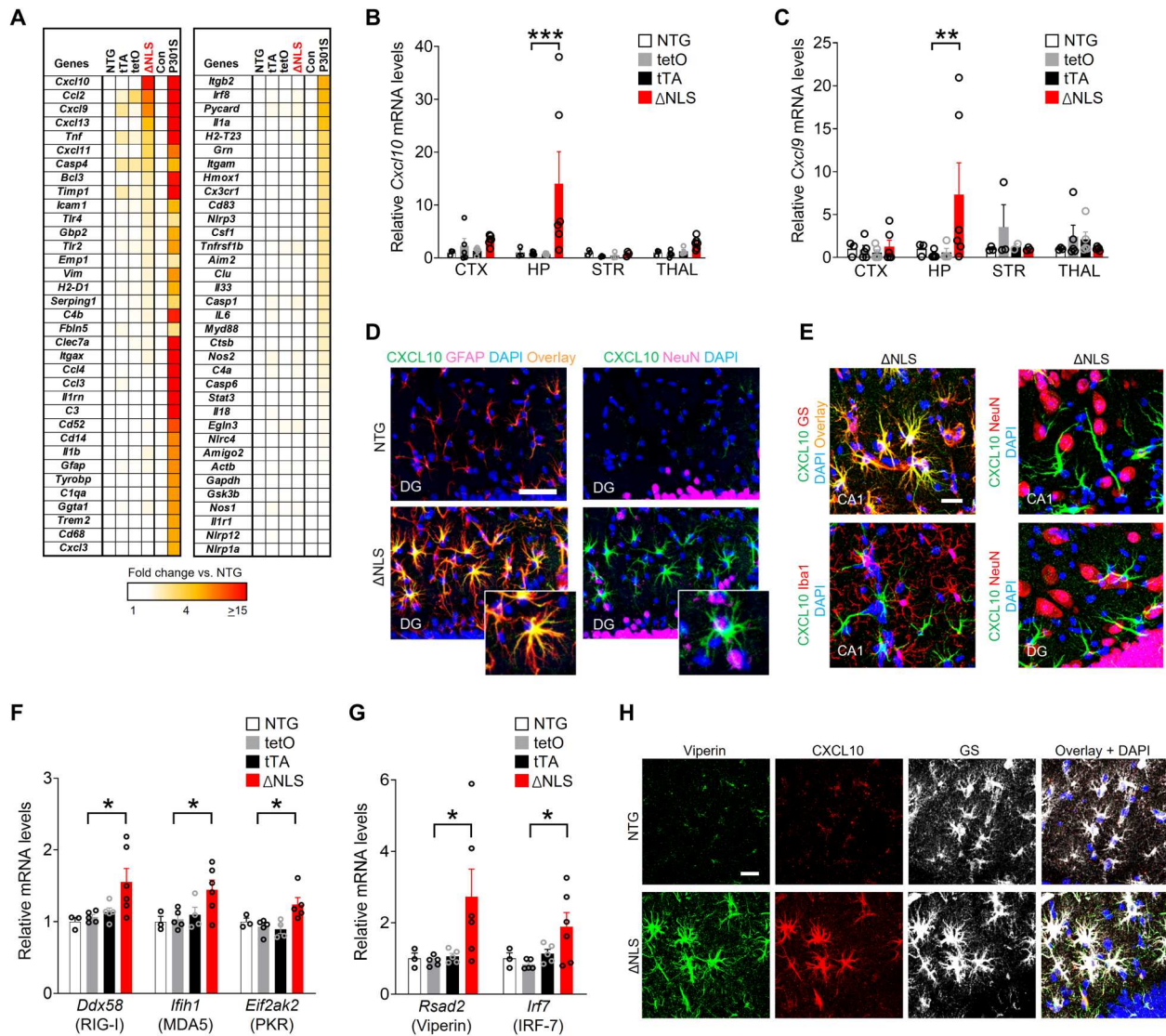
Fig. 4. Astrocytic TDP-43 alterations increase hippocampal IFN-inducible chemokines and other antiviral response factors. (**A**) Hippocampal RNA levels for indicated genes in 11-month-old littermate NTG controls, single transgenic *hGFAP*-tTA (tTA) and *tetO*–hTDP-43–ΔNLS (tetO) controls, and double transgenic hTDP-43–ΔNLS mice (ΔNLS). Transgenic tau-P301S mice (P301S) and their littermate controls at 10 months of age were used for validation and comparison of gene expression. (**B** and **C**) RNA levels from indicated brain regions as measured by RT-qPCR. Neocortex (CTX), hippocampus (HP), striatum (STR), and thalamus (THAL). Two-way ANOVA: $F_{(9,52)} = 2.06$, $P = 0.051$ for interaction and $F_{(3,52)} = 3.061$, $P = 0.019$ for genotype (B); $F_{(9,49)} = 1.65$, $P = 0.13$ for interaction and $F_{(3,49)} = 0.85$, $P = 0.47$ for genotype (C); Dunnett's post hoc test: **$P < 0.01$ and ***$P < 0.001$ versus tetO. (**D** and **E**) CXCL10 immunoreactivity (green) in the dentate gyrus molecular layer and CA1 of 11-month-old NTG and ΔNLS mice. Astrocyte markers GFAP or glutamine synthetase (GS), neuronal marker NeuN, or microglial/macrophage marker Iba1, as indicated. Yellow indicates overlay of green and red channels. DAPI (blue) was used to visualize nuclei. Insets in (D) show magnified views. Scale bars, 100 μm (D) and 20 μm (E). (**F** and **G**) Hippocampal RNA levels in 11-month-old NTG controls, single transgenic tetO and tTA controls, and ΔNLS mice. One-way ANOVA: $F_{(3,15)} = 4.19$, $P = 0.024$ (*Ddx58*); $F_{(3,14)} = 4.02$, $P = 0.029$ (*Ifih1*); $F_{(3,13)} = 5.097$, $P = 0.015$ (*Eif2ak2*); $F_{(3,15)} = 3.38$, $P = 0.046$ (*Rsad2*); and $F_{(3,15)} = 3.29$, $P = 0.049$ (*Irf7*). Dunnett's post hoc test: *$P < 0.05$ versus tetO. (**H**) Viperin (green), CXCL10 (red), and glutamine synthetase (white) immunoreactivity in the dentate gyrus of 11-month-old NTG and ΔNLS mice. Scale bar, 20 μm.

responses. Transfection with poly(I:C) induces robust astrocytic antiviral responses at least in part via toll-like receptor 3 and MDA5 (*75*). As expected, isolated astrocytes acutely transfected with poly(I:C) had robust induction of antiviral genes and reduced levels of infection by vesicular stomatitis virus (VSV), a negative-sense RNA virus (Fig. 6A and fig. S6A). In comparison to NTG controls, ΔNLS astrocytes had increased levels of VSV infection (Fig. 6A), suggesting that antiviral responses were impaired.

ΔNLS astrocytes also had increased infection by adenovirus (Fig. 6B), a dsDNA virus. Cell culture density was similar between treatments and genotypes (fig. S6, B and C), indicating that the observed increases in viral infections were unlikely to result from altered cell survival or proliferation. We also tested whether astrocytes were more susceptible to herpes simplex virus-1 (HSV-1), a highly neurotropic dsDNA virus increasingly implicated in AD (*76*, *77*). ΔNLS astrocytes had increased levels of HSV-1 infection

Fig. 5. Astrocytic TDP-43 has cell-autonomous effects on antiviral gene expression, neuroimmune pathways, and chemokine production. (**A** and **B**) Western blots of human TDP-43 or mouse and human TDP-43 levels (total TDP-43) in primary hippocampal astrocytes from NTG or ΔNLS mice. TDP-43 levels were normalized to γ-tubulin. Student's *t* test with Welch's correction: ***$P < 0.001$ versus NTG. (**C** and **D**) RNA levels in primary hippocampal astrocytes. Student's *t* test: *$P < 0.05$ and **$P < 0.01$ versus NTG. (**E** and **F**) CXCL10 protein levels in lysates (E) and medium (F) from primary hippocampal astrocytes as measured by enzyme-linked immunosorbent assay (ELISA). **$P < 0.01$ and *$P < 0.05$. (**G**) IFN-γ protein levels in lysates from primary hippocampal astrocytes. *$P < 0.05$. (**H** and **I**) Western blots of phosphorylated and total NF-κB and β-actin in primary hippocampal astrocytes. Student's *t* test with Welch's correction: **$P < 0.01$. (**J** and **K**) *Cxcl10* (J) and *Cxcl9* (K) mRNA levels in primary hippocampal astrocytes. Vehicle [Veh; dimethyl sulfoxide (DMSO)], Stattic (5 μM, 24 hours), or SN50 (10 μM, 24 hours). One-way ANOVA: $F_{(3,30)} = 12.74$, $P < 0.0001$ (*Cxcl10*) and $F_{(3,28)} = 4.39$, $P = 0.012$ (*Cxcl9*). Dunnett's post hoc test: ***$P < 0.001$ and *$P < 0.05$ versus ΔNLS/vehicle. **$P < 0.01$. (**L** and **M**) Western blot quantification of human TDP-43 (L) and total TDP-43 (M) protein levels in hippocampal astrocytes from ΔNLS mice. Cultures were maintained in DOX (2 μg/ml)–containing or control medium. Student's *t* test with Welch's correction: ***$P < 0.001$. (**N**) *Cxcl10* mRNA levels in primary hippocampal astrocytes. Some astrocytes were maintained in DOX-containing medium and analyzed at DIV (days in vitro) 8 or 12. Two-way ANOVA: $F_{(1,11)} = 14.62$, $P = 0.0028$ for interaction/DIV 8 and $F_{(1,24)} = 8.28$, $P = 0.0083$ for interaction/DIV 12. Bonferroni post hoc test: ***$P < 0.001$. (**O**) Western blot quantification of phosphorylated NF-κB and STAT3 levels in primary hippocampal astrocytes. Normalized to total levels of each protein. One-way ANOVA: $F_{(2,10)} = 29.53$, $P < 0.0001$ (pNF-κB/ ΔNLS); $F_{(2,10)} = 13.68$, $P = 0.0014$ (pSTAT3/ ΔNLS); $F_{(2,6)} = 1.77$, $P = 0.25$ (pNF-κB/NTG); and $F_{(2,6)} = 0.20$, $P = 0.83$ (pSTAT3/NTG). Dunnett's post hoc test: ***$P < 0.001$.
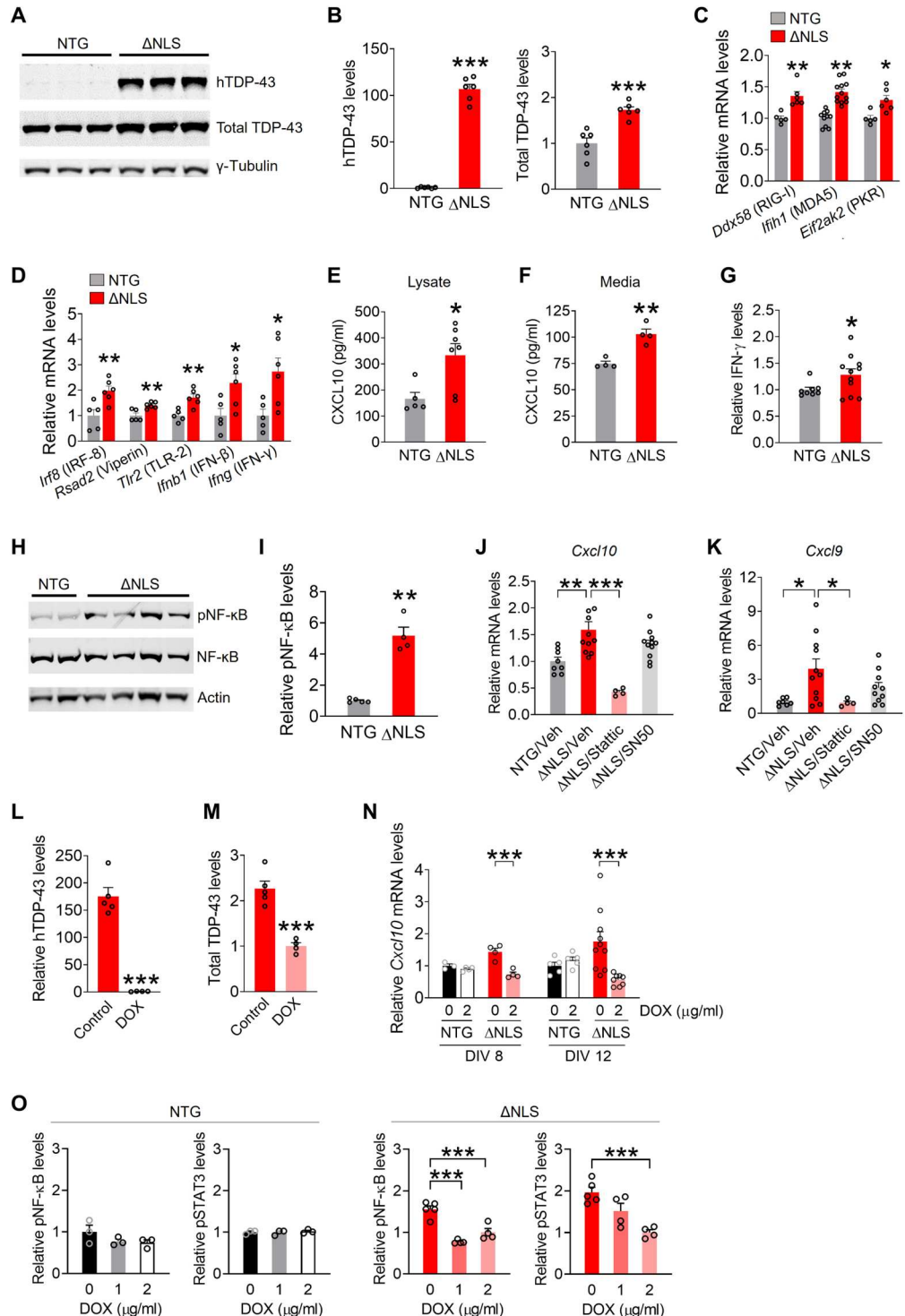
(Fig. 6, C to E). Thus, in addition to affecting cognitive function, alterations in astrocytic TDP-43 impaired antiviral defenses, which may predispose the cells to infectious pathogens. However, further studies are necessary to address how astrocytic proteinopathy affects host responses to microbial pathogens and possibly other neuroimmune challenges and whether alterations in type I and/or type II IFN pathways or other mechanisms, such as metabolic alterations (*78*), are contributing factors.
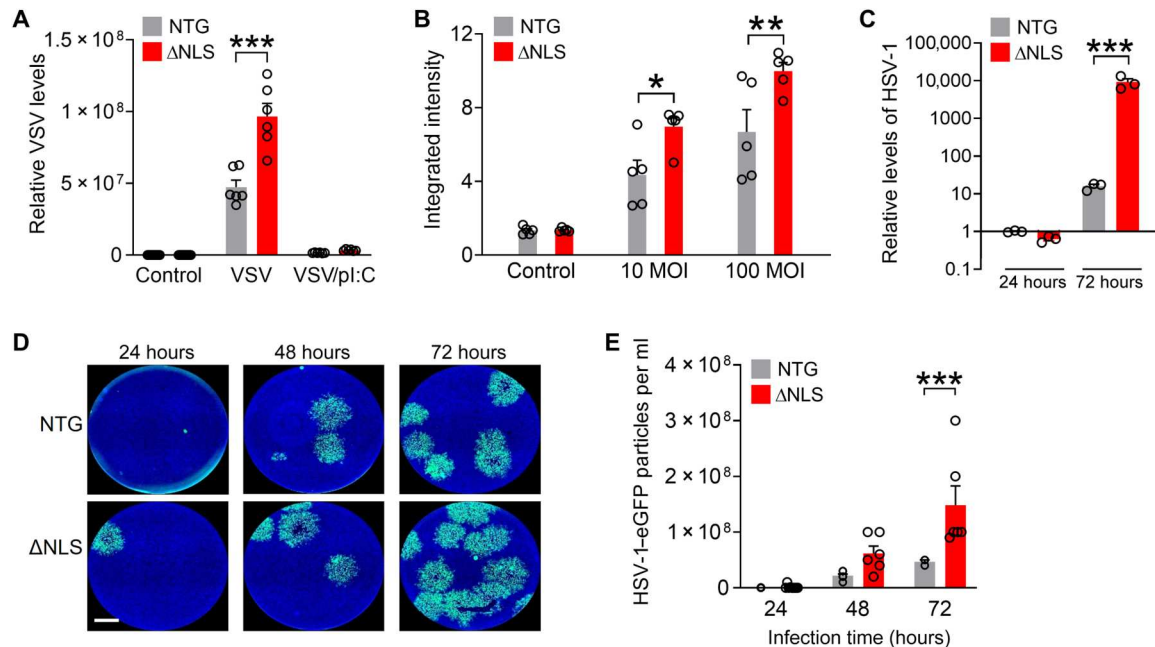
Fig. 6. Astrocytic TDP-43 affects antiviral defenses in a cell-autonomous manner. (**A**) Primary astrocytes from NTG and ΔNLS mice were infected with VSV [100 multiplicity of infection (MOI)] for 24 hours. Some wells were also transfected with poly(I:C) (pI:C). VSV levels were measured by RT-qPCR. Two-way ANOVA: $F_{(2,41)} = 34.64$, $P < 0.0001$ for interaction and $F_{(1,41)} = 40.60$, $P < 0.0001$ for genotype. Bonferroni post hoc test: ***$P < 0.001$ versus NTG. (**B**) Primary astrocytes were infected with adenovirus tagged with enhanced green fluorescent protein (eGFP) at indicated MOIs for 24 hours. eGFP levels were measured by quantitative microscopy. $F_{(2,24)} = 3.47$, $P = 0.047$ for interaction and $F_{(1,24)} = 13.73$, $P = 0.0011$ for genotype. Bonferroni post hoc test: *$P < 0.05$ and **$P < 0.001$ versus NTG. (**C**) Primary astrocytes were infected with HSV-1 tagged with eGFP (0.01 MOI) for 24 or 72 hours. Glycoprotein B (gB) DNA levels were normalized to 18S DNA per sample. Two-way ANOVA: $F_{(1,12)} = 15.66$, $P = 0.0019$ for genotype and $F_{(2,12)} = 9.225$, $P = 0.0037$ for interaction. Bonferroni's post hoc test: ***$P = 0.0003$ versus NTG for 72 hours. (**D** and **E**) Conditioned medium was collected from primary NTG or ΔNLS astrocytes after infection with HSV-1–eGFP (0.01 MOI). Astrocytes were washed 3 hours after infection, and conditioned medium was analyzed after indicated durations using the plaque assay in Vero cells. (D) Representative images of Vero cells after treatment with conditioned medium from NTG or ΔNLS astrocytes that were infected with HSV-1–eGFP for indicated durations. Scale bar, 1200 μm. (E) Viral particles in conditioned medium from HSV-1–infected NTG or ΔNLS astrocytes. Two-way ANOVA: $F_{(1,33)} = 15.24$, $P = 0.0004$ for genotype and $F_{(2,33)} = 5.58$, $P = 0.0082$ for interaction. Bonferroni's post hoc test: ***$P = 0.0009$ versus NTG for 72 hours.

Astrocytic TDP-43 alterations are linked to increased presynaptic levels of the chemokine receptor CXCR3 and CXCR3-mediated neuronal impairments

Given that memory was impaired in ΔNLS mice, we next explored how changes in astrocytic IFN-inducible factors might affect neuronal functions. Upon release, IFN-inducible chemokines CXCL9 to CXCL11 activate the shared G protein–coupled receptor CXCR3 (*79*), which can be expressed by neurons (*62*), microglia (*80*), and potentially other cell types. Notably, patients with FTD or AD show increased levels of CXCL10 (*81*) and have hippocampal CXCR3 expression predominantly in neurons (*62*), suggesting that neuronal CXCR3 might play a role in these disorders. We found that hippocampal *Cxcr3* RNA and protein levels were increased in ΔNLS mice (Fig. 7, A and B, and fig. S7A) and the majority of CXCR3-immunoreactive puncta were localized in neurons (Fig. 7, C and D). However, ΔNLS mice did not have increased levels of CXCR3 immunoreactivity within neuronal cell bodies (Fig. 7, C and D). Coimmunolabeling for CXCR3 and different presynaptic and postsynaptic markers revealed that ΔNLS mice had twofold increases in CXCR3 selectively within synaptophysin-positive puncta, but not within Postsynaptic density protein-95 (PSD-95) or gephyrin-positive puncta (Fig. 7, E to H, and fig. S7B), suggesting that the increases in hippocampal CXCR3 levels were localized to presynaptic terminals.

CXCR3 activation triggers $G_{i/o}$-coupled signaling, which can inhibit presynaptic neurotransmitter release (*82*, *83*). However, the presynaptic effects of CXCR3 have not been previously defined. Thus, we next assessed whether activation of presynaptic CXCR3 affects neuronal activity using the multielectrode array (MEA) system. For these experiments, primary mouse neurons were transduced with PHP.eB AAV *Syn1-Cxcr3*-2HA–neurexin-1α. In this vector, the neurexin-1α sequence targets CXCR3 to presynaptic terminals, which simulates the presynaptic enrichment of CXCR3 observed in ΔNLS mice and limits artificial effects of CXCR3 on neuronal excitability (*84*). We confirmed that the vector was functional in neurons and that CXCR3 stimulation with chemokines induced characteristic intracellular signaling (fig. S7, C and D). We found that acute chemokine treatment inhibited spontaneous neuronal activity within minutes of treatment (Fig. 8A), suggesting that CXCR3 rapidly suppresses neuronal firing, possibly through modulation of calcium channels and presynaptic vesicles (*82*, *83*).

In contrast to the acute effects, chronic stimulation of CXCR3 increased spontaneous neuronal activity (Fig. 8B), indicating that CXCR3 also promotes long-lasting increases in neuronal firing, likely through chronic changes in the presynaptic compartment. Chronic stimulation of CXCR3 enhanced the levels of synaptophysin-positive puncta, a marker of presynaptic vesicles, but did not
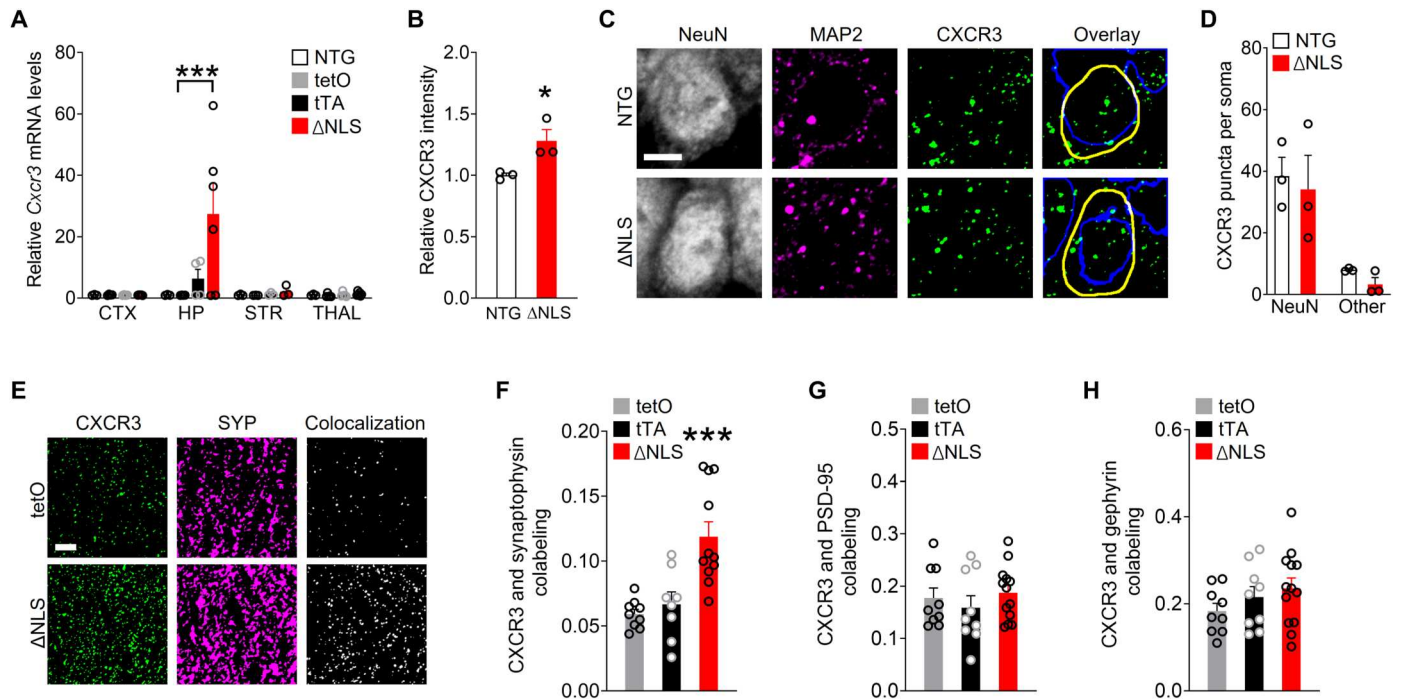
Fig. 7. Astrocytic TDP-43 alterations increase chemokine receptor CXCR3 levels in presynaptic terminals. (**A**) *Cxcr3* RNA levels from indicated brain regions of NTG, single transgenic controls (tetO and tTA), and double transgenic ΔNLS mice. Neocortex, hippocampus, striatum, and thalamus. Two-way ANOVA: $F_{(9,48)} = 2.89$, $P = 0.0081$ for interaction and $F_{(3,48)} = 2.93$, $P = 0.043$ for genotype; Dunnett's post hoc test: ***$P < 0.001$ versus tetO. (**B** and **D**) Images [C Microtubule-associated protein 2(MAP 2)] and quantification (B and D) of hippocampal immunoreactivity for CXCR3 in the CA1 radiatum parenchyma (B) or specifically in CA1 neuronal cell bodies (**C** and **D**) as delineated by coimmunolabeling with neuronal marker NeuN versus non-NeuN regions in NTG and ΔNLS mice. Neuronal nuclei are indicated by blue traces; cell somas are indicated by yellow traces. Arbitrary fluorescence intensity units were normalized to NTG mice (B). Student's *t* test: *$P = 0.039$. (**E** and **F**) Colocalization of CXCR3 and the presynaptic marker synaptophysin in the CA1 region of single transgenic controls and ΔNLS mice. Mander's overlap coefficient was used to assess colocalization. One-way ANOVA: $F_{(2,25)} = 12.94$, $P < 0.0001$; Dunnett's post hoc test: ***$P < 0.001$ versus tetO. (**G** and **H**) Colocalization of CXCR3 and the postsynaptic markers PSD-95 (G) or gephyrin (H) in the CA1 region of single transgenic controls and double transgenic ΔNLS mice. Mander's overlap coefficient was used to assess colocalization. Scale bars, 5 μm (C, E).

affect PSD-95, a marker of postsynaptic compartments (Fig. 8, C and D, and fig. S7E). Notably, neurons transduced with AAV-CXCR3, but not treated with chemokines, and neurons treated with chemokines, but not transduced with AAV-CXCR3, performed similarly to untransduced vehicle-treated control neurons, ruling out nonspecific effects of the AAV vector and treatment on neuronal responses.

To test whether similar presynaptic changes were present in the hippocampus of ΔNLS mice, we compared the levels of different synaptic markers by quantitative immunofluorescence. Similar to neuronal cultures overexpressing presynaptic CXCR3, double transgenic ΔNLS mice had increased levels of synaptophysin-positive puncta (Fig. 8, E and F) without marked changes in the levels of PSD-95 or gephyrin, which are markers of excitatory and inhibitory postsynaptic zones, respectively (fig. S7, F and G). There were also no detectable changes in the levels of bassoon, a scaffolding protein in excitatory and inhibitory presynaptic compartments, and no changes in synaptotagmin-2, a marker of inhibitory presynaptic vesicles (fig. S7, H and I) (*85*). Thus, astrocytic TDP-43 modulates excitatory presynaptic compartments without markedly changing the density of synapses.

We next investigated whether astrocytic TDP-43 altered functional electrophysiological readouts of hippocampal transmission and presynaptic release. For these experiments, acute hippocampal slices were obtained from double transgenic ΔNLS mice or littermate controls at 5 to 6 months of age. The Schaffer collateral pathway was stimulated while recordings of field excitatory postsynaptic potentials (fEPSPs) were obtained in the striatum radiatum of the dorsal CA1 region. We found that ΔNLS mice had increased basal synaptic transmission as evidenced by enhanced fEPSPs (Fig. 8G). This effect was most apparent at higher stimulus intensities. The mice also had impaired paired-pulse facilitation, as reflected by lower fEPSP2/fEPSP1 ratios (Fig. 8H). Notably, ΔNLS mice had increased responses to the first but not second pulses as compared to control mice (Fig. 8, I and J), indicative of enhanced probability of neurotransmitter release, which likely contributed to the observed increases in basal synaptic transmission. No significant differences were detected in fiber volley amplitudes, which reflect presynaptic action potentials, or in linear regressions of fEPSP slopes and fiber volleys (fig. S7, J and K).

To further test whether the presence of astrocytes with TDP-43 alterations is sufficient to affect neuronal activities and to confirm that this effect is not dependent on other cell types, we generated primary astrocytic-neuronal cocultures in which neurons were derived from NTG mice and astrocytes were derived from transgenic *Aldh1l1*-Cre mice to enable astrocyte-selective transgene expression. Before the addition of neurons to the cultures, isolated *Aldh1l1*-Cre astrocytes were transduced with a PHP.eB AAV

Fig. 8. Astrocytic TDP-43 and neuronal CXCR3 promote hyperexcitability and aberrant presynaptic function. (**A** to **D**) Primary neurons transduced with AAV PHP.eB-*Syn-Cxcr3*-hemagglutinin–neurexin-1α. Control cultures were not transduced. (A) CXCL11 (CXL; 200 nM) or vehicle applied after a 30-min baseline. Firing rates at 1 min after stimulation (normalized to baseline). Two-way ANOVA: $F_{(1,45)} = 8.38$, $P = 0.0058$ for interaction and $F_{(1,45)} = 5.83$, $P = 0.02$ for CXCL11. Bonferroni's test: **$P < 0.01$ versus vehicle. (B) CXCL11 (200 nM) or vehicle was applied chronically (24 hours) after a 30-min baseline. (C and D) Quantification (C) and images (D) of the presynaptic marker synaptophysin in neurons treated chronically (3 days) with CXCL11 (200 nM) or vehicle. Two-way ANOVA: $F_{(1,50)} = 8.85$, $P = 0.0045$ for interaction (firing rate); $F_{(1,50)} = 11.73$, $P = 0.0012$ for CXCL11 (firing rate); $F_{(1,36)} = 8.65$, $P = 0.0057$ for interaction (area); and $F_{(1,36)} = 6.24$, $P = 0.017$ for interaction (counts). Bonferroni's test: **$P < 0.01$ and ***$P < 0.001$ versus vehicle. Scale bar, 50 μm. (**E** and **F**) Synaptophysin in the CA1 radiatum of single transgenic controls and ΔNLS mice. One-way ANOVA: $F_{(2,26)} = 9.94$, $P = 0.0006$ (E) and $F_{(2,26)} = 11.62$, $P = 0.0002$ (F); Dunnett's post hoc test: ***$P < 0.001$ versus tetO. (**G** and **H**) Recordings in hippocampal slices from controls and ΔNLS mice at 5 to 6 months of age. (G) Basal transmission at increasing stimulus intensities. Mixed-effects model: $F_{(7,344)} = 2.10$, $P = 0.043$ for interaction and $F_{(1,50)} = 4.19$, $P = 0.046$ for genotype. (H) Paired-pulse facilitation (ratios of fEPSPs to the second pulse as compared to the first pulse). Mixed-effects model: $F_{(6,338)} = 2.43$, $P = 0.026$ for interaction and $F_{(1,60)} = 7.81$, $P = 0.007$ for genotype. Bonferroni's test: *$P < 0.05$. (**I** and **J**) fEPSPs in response to the first (I) and second (J) stimulus independent of interval. Student's *t* test: ***$P < 0.001$. (**K** and **L**) Primary neurons cocultured with hippocampal *Aldh1l1*-Cre astrocytes that were transduced with AAV PHP.eB-*hGfaABC₁D*-DIO–hTDP-43–ΔNLS (ΔNLS) or AAV PHP.eB pAAV-FLEX-tdTomato. One-way ANOVA: $F_{(2,25)} = 15.93$, $P < 0.0001$ (K). CXCR3 blocker SCH 546738 (12 nM). Dunnett's test: ***$P < 0.001$. Student's *t* test: ***$P = 0.0003$.
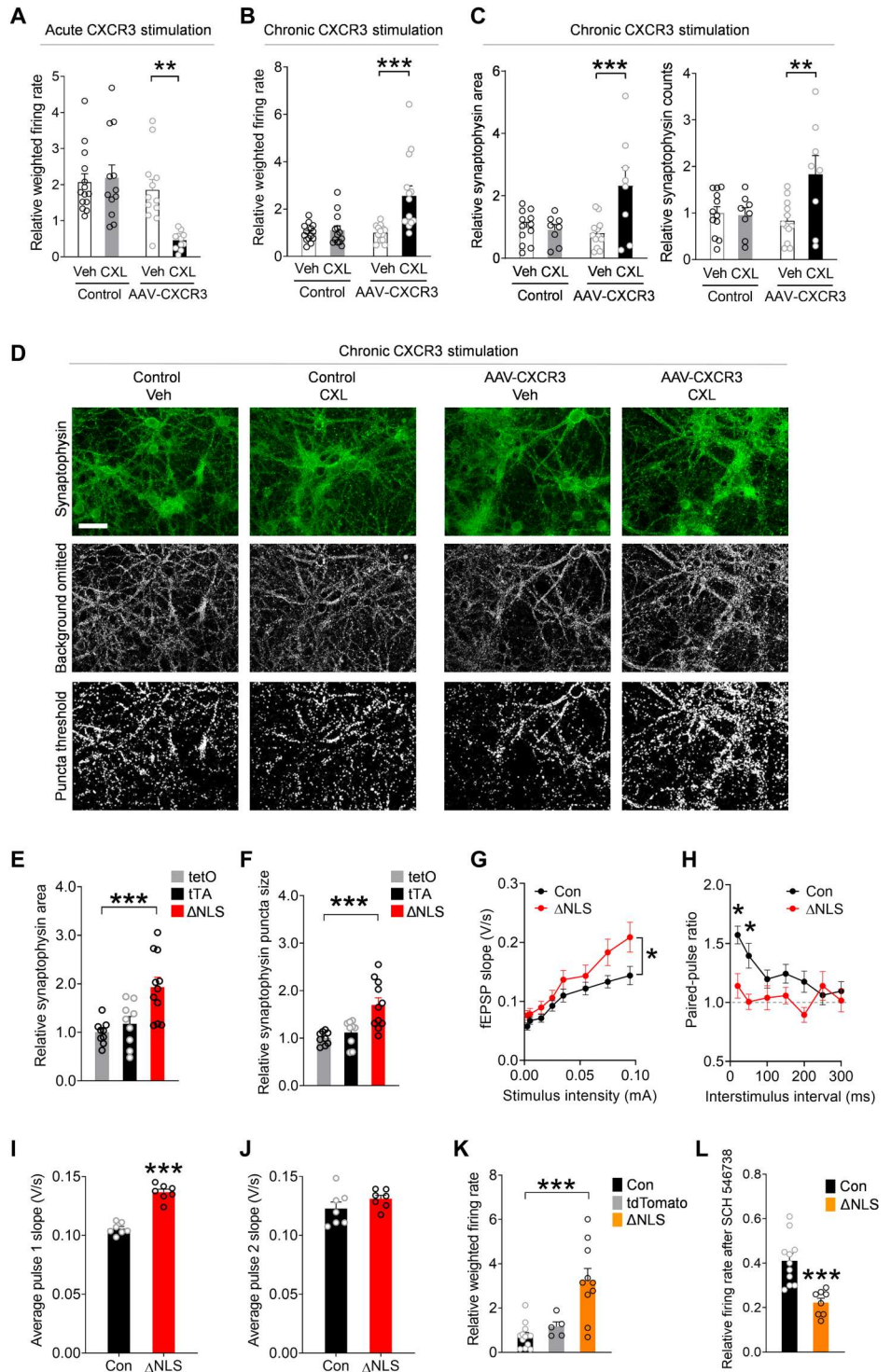
vector encoding Cre-dependent hTDP-43–ΔNLS under the control of the *hGfaABC₁D* promoter. Consistent with our findings in ΔNLS mice, NTG neurons cocultured with *Aldh1l1*-Cre astrocytes expressing hTDP-43–ΔNLS had altered spontaneous firing patterns as compared to neurons cocultured with control *Aldh1l1*-Cre astrocytes (Fig. 8K). Notably, spontaneous neuronal activities were suppressed by selective blockade of CXCR3 with SCH 546738 (12 nM)

to approximately 40% of baseline activities, and this suppressive effect was significantly more pronounced in neurons cultured in the presence of hTDP-43–ΔNLS–expressing astrocytes (Fig. 8L), revealing an increased involvement of CXCR3. Together with our findings in isolated neurons and hippocampal slices, these results suggest that astrocytic TDP-43 is linked to CXCR3-dependent neuronal hyperactivity.

Given these findings, astrocytic TDP-43 alterations may promote memory loss in part through CXCR3-induced effects on hippocampal function. Thus, we next tested whether genetic ablation of the gene encoding CXCR3 can prevent TDP-43–related memory loss. For these experiments, we generated *Aldh1l1*-Cre mice that were either WT or functional null (KO) for *Cxcr3* and performed bilateral injections of the PHP.eB AAV vector encoding hTDP-43–ΔNLS into the hippocampal formation at 4 to 9 months of age (Fig. 9, A and B). Given that *Cxcr3* is X-linked, we used littermate male mice that were either WT or KO for *Cxcr3* and expressed Cre recombinase, which enabled cell-selective hTDP-43 expression in hippocampal astrocytes. The mice were then assessed in the Morris water maze at 7 to 12 months of age.

Similar to other results (Fig. 3), *Aldh1l1*-Cre/*Cxcr3*-WT mice that received AAV vector encoding hTDP-43–ΔNLS had impaired memory as compared to control mice that lacked hTDP-43–ΔNLS (Fig. 9, C to F), without changes in swim speeds (Fig. 9G). In contrast, *Aldh1l1*-Cre/*Cxcr3*-KO mice with hTDP-43–ΔNLS performed more similarly to control mice lacking hTDP-43–ΔNLS (Fig. 9, D to F), suggesting that alterations in astrocytic TDP-43 cause memory loss in a CXCR3-dependent manner. In addition, under control conditions, the behavior of *Aldh1l1*-Cre/*Cxcr3*-KO mice was not different from *Aldh1l1*-Cre/*Cxcr3*-WT mice, suggesting that CXCR3 impairs memory upon changes in astrocytic function. Together, our study reveals that astrocytic TDP-43 pathology is linked to maladaptive antiviral changes and increased chemokine signaling that disrupts hippocampal synaptic transmission and contributes to memory loss (Fig. 10).

DISCUSSION

Memory loss is common in aging-related neurological disorders, including AD, ALS-FTD, hippocampal sclerosis, and other conditions. However, the exact causes of memory loss are not clear and
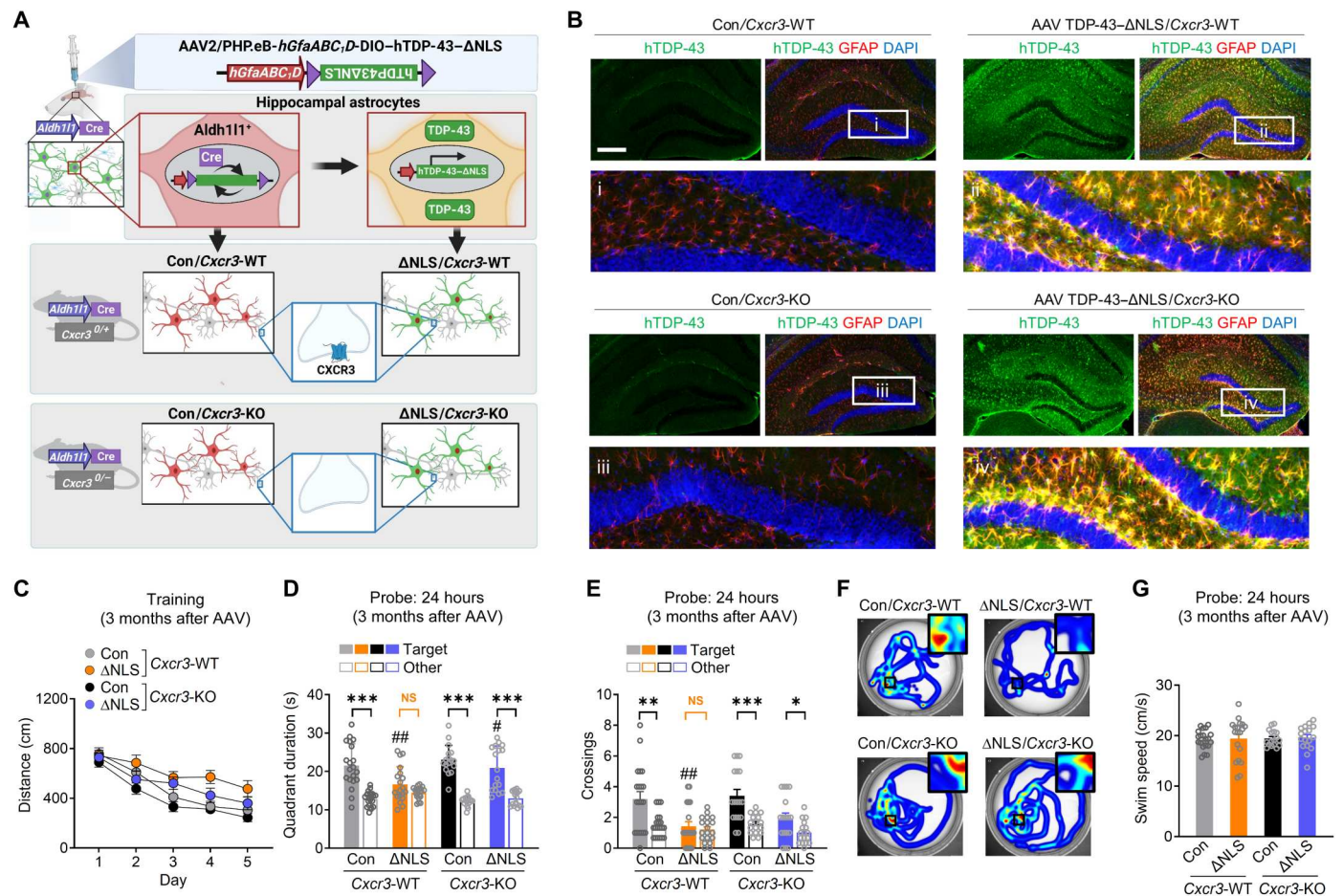

Fig. 9. Ablation of CXCR3 alleviates astrocytic TDP-43–linked memory deficits. (**A**) Experimental design. Transgenic *Cxcr3*-WT or *Cxcr3*-KO male mice on a *Aldh1l1*-Cre background were injected with AAV PHP.eB-*hGfaABC₁D*-DIO–hTDP-43–ΔNLS (ΔNLS) or saline (Con) at 4 to 9 months of age and tested in the Morris water maze at 7 to 12 months of age. Control AAV injections in NTG mice are shown in Fig. 3 and fig. S4. (**B**) hTDP-43 (green) and the astrocytic marker GFAP (red). DAPI (blue) was used to visualize nuclei. Yellow indicates overlay of green and red channels. Insets i to iv show magnified views. Scale bar, 300 μm. (**C**) Distance traveled during hidden platform training. Mixed-effects model: $F_{(1,70)} = 17.84$, $P < 0.0001$ for ΔNLS; $F_{(1,70)} = 8.93$, $P = 0.0039$ for *Cxcr3*-KO; $F_{(1,70)} = 0.12$, $P = 0.73$ for ΔNLS–*Cxcr3*-KO interaction. (**D** to **G**) Probe trial 24 hours after training. Durations in target and nontarget (other) quadrants. Two-way ANOVA (target): $F_{(1,69)} = 8.82$, $P = 0.004$ for ΔNLS; $F_{(1,69)} = 5.94$, $P = 0.017$ for *Cxcr3*-KO (D); and $F_{(1,69)} = 16.3$, $P = 0.0001$ for ΔNLS (E). Bonferroni's test: ##$P < 0.01$ versus control/*Cxcr3*-WT and #$P < 0.05$ versus ΔNLS/*Cxcr3*-WT. Student's *t* test with Welch's correction: ***$P < 0.001$, **$P < 0.01$, and *$P < 0.05$ versus other. (F) Swim paths during the probe trial; insets show magnified views of the target platform area. (G) Swim speeds in the 24-hour probe trial.
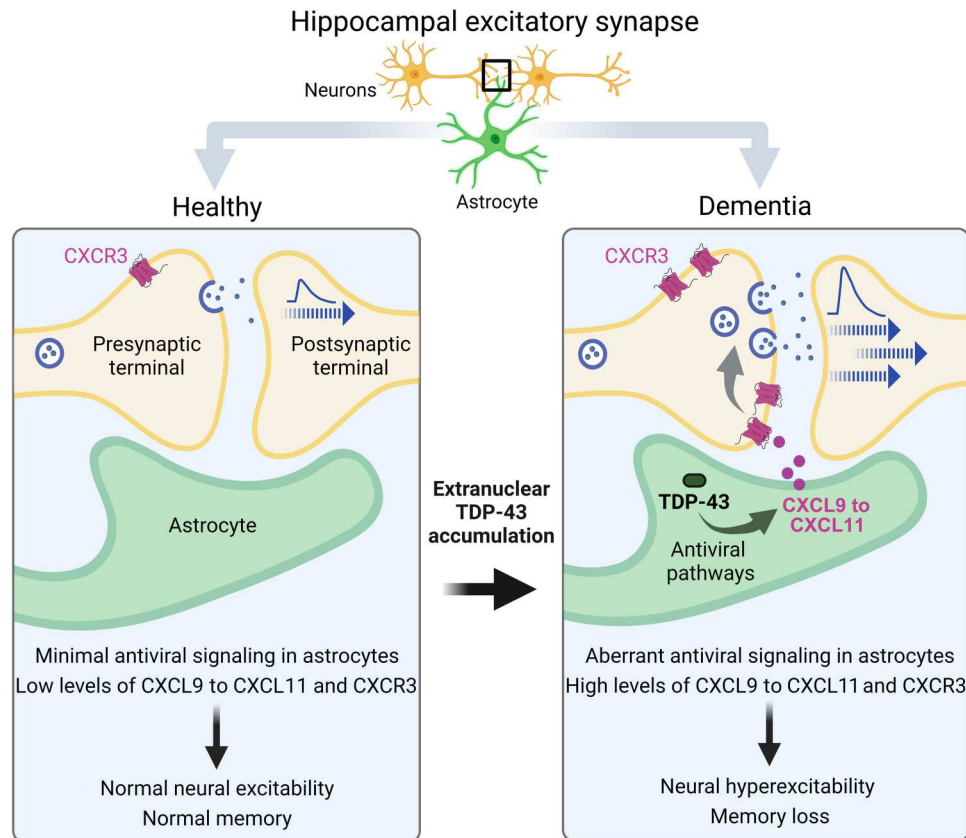
Fig. 10. Summary of the main findings. In AD and FTD, hippocampal astrocytes had aberrant accumulation of cytoplasmic TDP-43. These alterations were linked to brain region–specific and cell-autonomous changes in astrocytic antiviral pathways and increased production of IFN-inducible chemokines. The corresponding chemokine receptor CXCR3 was increased selectively in hippocampal excitatory presynaptic terminals and promoted neuronal hyperactivity and memory loss. Thus, dementia-associated TDP-43 dysregulation in astrocytes causes chemokine-mediated changes in excitatory transmission leading to cognitive deficits.

treatment options are limited. Increasing evidence implicates glial dysfunction and abnormal glial-neuronal interactions in various pathophysiological processes (*35–37*). In particular, astrocytes have been implicated in various central nervous system (CNS) disorders (*86–89*) and, similar to neurons, are functionally diverse (*90, 91*) and affect information processing (*57*). Aberrant changes in astrocytes can contribute to behavioral and cognitive deficits and promote memory loss associated with aging and disease (*39, 57, 92*). However, the mechanisms by which astrocytes impair memory and other cognitive processes are not fully defined.

Here, we demonstrate that human hippocampal astrocytes accumulate extranuclear TDP-43 in AD and FTD. Astrocytic TDP-43 accumulation in the hippocampus was sufficient to impair memory, but not other neurocognitive functions, and it altered hippocampal neural activity and presynaptic function. Consistent with the selective impairments in memory, we detected marked increases in IFN-inducible chemokines preferentially in hippocampal astrocytes and increases in the corresponding chemokine receptor CXCR3 in hippocampal presynaptic terminals. These findings suggest that astrocytes in the hippocampus have a distinct response to TDP-43 alterations as compared to astrocytes in other brain regions. Widespread and chronic transgene expression in astrocytes did not cause motor impairments, early mortality, or other severe deficits. In contrast, animal models with analogous TDP-43

manipulations in neurons have severe ALS-associated phenotypes, including motor impairments and early mortality (*18*). These distinct and selective effects suggest that responses to TDP-43 accumulation are cell type–specific and heterogeneous across astrocytes in different brain regions.

Similar to TDP-43, ALS-linked mutations in superoxide dismutase (SOD1) cause neurotoxicity, motor impairments, and early mortality. Analogous to our findings, astrocyte-targeted expression of mutant SOD1 is not sufficient to trigger onset of motor neuron disease in mice (*93*). However, astrocytic SOD1 is required for disease progression, and astrocytes carrying mutant SOD1 are selectively damaging to isolated motor neurons but not other neuronal subtypes (*94, 95*). Similarly, AD-linked tau accumulation in hippocampal astrocytes promotes selective neuronal deficits (*96*). Together, our findings and previous work indicate that various dementia-linked protein alterations in astrocytes cause highly context-dependent effects on neurons and might facilitate selective neuronal vulnerability that contributes to variable disease manifestations in neurodegenerative conditions.

Most dementia cases involve dysregulation of WT rather than mutant TDP-43. Overexpression of WT TDP-43 in model systems is sufficient to impair cell function at least in part through the effects of TDP-43 outside the nucleus (*54*). We found that expression of either hTDP-43–WT or hTDP-43–ΔNLS, but not

control proteins targeted to hippocampal astrocytes, induced progressive memory deficits, suggesting that even modest alterations in WT TDP-43 within hippocampal astrocytes can impair memory and contribute to dementia-associated cognitive decline. Hippocampal astrocytes were not similarly vulnerable to control vectors, thus ruling out nonspecific effects of AAV injections or chronic protein overexpression as major drivers of the observed phenotype. Notably, microglia and other neural cells in the hippocampus might indirectly modulate astrocytic functions and the effects of TDP-43 alterations. Microglial progranulin and Triggering receptor expressed on myeloid cells 2 (TREM2) insufficiency may contribute to TDP-43 pathology (55, 97).

Astrocytic TDP-43 alterations were accompanied by cell-autonomous changes in antiviral gene expression, increased phosphorylation of NF-κB and STAT3, increased levels of IFN-γ, release of chemokines, and functional changes in astrocytic innate defense against viral pathogens. Together, these results point to an aberrant TDP-43–linked antiviral phenotype (aTAP) that may affect cognitive function and neuroimmune responses. Our study focused on astrocytes, but TDP-43 is present in most cell types and increasingly linked to IFN-related pathways in different cell populations (98, 99), suggesting that aTAP is not specific to astrocytes. TDP-43 accumulation in neurons triggers the antiviral cGAS-STING pathway, at least partly through abnormal mitochondrial DNA release (54). We did not detect changes in astrocytic cGAS or STING genes, possibly because aTAP engages distinct mechanisms in different cell types. Antiviral signaling involves multiple dynamic and cell-specific mechanisms (100). TDP-43 can also affect retrotransposon activity (101, 102), which may also contribute to aTAP. Thus, TDP-43 likely influences multiple intracellular targets that affect neuroimmune signaling and antiviral cascades.

Although we focused primarily on the neurocognitive effects, our results in isolated cells implicate TDP-43 in modulating innate responses to viral pathogens. A link between dementia and viral infections has been suggested (103–105), but the effects of TDP-43 pathology on neural responses to infections are not known. We tested three different viral pathogens, used several independent methods to measure viral infections, and assessed different time points and viral doses. Convergent results across these different conditions suggest that alterations in TDP-43 allow pathogens to exploit weaknesses in astrocytic antiviral responses, which might affect innate immunity in the brain.

IFN-related pathways in astrocytes and other neural cells modulate brain function and have been implicated in AD, ALS-FTD, and other CNS disorders (66, 69, 70, 106–109), but the roles of TDP-43 in these pathways have not been fully elucidated. We found that alterations in TDP-43 increased astrocytic IFN-inducible chemokines, among other genes, and promoted presynaptic increases in neuronal CXCR3, the shared receptor that is likely overactivated by the increased levels of chemokines. Although previous studies have reported CXCR3 expression in microglia (110) and infiltrating immune cells (111), we did not detect increases in CXCR3 in non-neuronal areas within the hippocampus. Similar to our results, CXCR3 has been detected in human neurons and neuronal processes (62). Acute activation of presynaptic CXCR3 suppressed neuronal activity, whereas chronic activation of CXCR3 increased neuronal activity. In a similar manner, neurons maintained in the presence of astrocytes with chronic TDP-43 accumulation had increased spontaneous neuronal activity, which was reduced by

pharmacological inhibition of CXCR3. These results suggest that alterations in astrocytic TDP-43 promote CXCR3-dependent neuronal hyperactivity. Moreover, we found that alterations in astrocytic TDP-43 affected presynaptic function without changing the number of synaptic zones. Our findings are consistent with recent studies showing that $G_{i/o}$-coupled receptors can enhance the number of presynaptic vesicles without altering the number of synapses (112). One mechanism promoting this effect may be presynaptic cyclic AMP (cAMP)/protein kinase A–dependent phosphorylation of synapsin-1, which results in the removal of vesicles from presynaptic clusters (112). Chronic activation of presynaptic $G_{i/o}$-coupled CXCR3 may reduce synapsin-1 phosphorylation and allow additional vesicle recruitment to active zones, thus facilitating presynaptic neurotransmitter release. In support, ΔNLS mice had increases in hippocampal transmission and presynaptic release probability, which may promote an abnormal shift to low-pass filtering of excitatory firing and thereby impair the encoding of spatial memory within the hippocampus. Genetic ablation of CXCR3 alleviated memory deficits but did not affect memory in mice without astrocytic TDP-43 manipulation. Thus, alterations in astrocytic TDP-43 cause neural hyperexcitability and memory deficits that are dependent on CXCR3.

These findings implicate blockers of chemokines and CXCR3 as potential therapeutic interventions for TDP-43–associated cognitive impairments. Notably, human CXCL10 levels are increased in progranulin-linked FTD (81), AD (113), and amnestic mild cognitive impairment (113), either in the cerebrospinal fluid or in astrocytes (62), and these levels correlate with cognitive performance (113). Moreover, neural hyperexcitability has been reported in dementia (114), and global KO of CXCR3 prevents memory deficits in transgenic mice with amyloid-β pathology (115). CXCR3 blockers have reached clinical trials for peripheral inflammatory conditions (116) but have not yet been tested in patients with dementia or other cognitive disorders.

In summary, our findings suggest that TDP-43 alterations in astrocytes contribute to cognitive decline in dementia. We describe a previously unknown chemokine-mediated mechanism that is likely downstream of astrocytic TDP-43–linked antiviral changes that affects hippocampal presynaptic function and neuronal activities. Together, our results implicate astrocytic TDP-43 impairments and aTAP in dementia pathogenesis and point to chemokine signaling as a potential therapeutic target.

MATERIALS AND METHODS
Mice
All animal experiments were conducted in accordance with guidelines set by the Institutional Animal Care and Use Committee of Weill Cornell Medicine. Mice were housed in groups of two to five mice per cage and maintained on a 12-hour light/dark cycle with ad libitum access to food and water. Experiments were conducted during the light cycle and included littermate controls. Regulatable and astrocyte-specific expression of hTDP-43 was achieved using transgenic hGFAP-tTA mice with a tet-off tTA element downstream of the human GFAP (hGFAP) promoter (provided by L. Mucke, Gladstone Institutes, San Francisco, CA) (39). hGFAP-tTA mice [B6.Cg-Tg(GFAP-tTA)110Pop/J; the Jackson Laboratory, strain #005964] were crossed with tetO–hTDP-43–ΔNLS mice [B6;C3-Tg(tetO-TARDBP*)4Vle/J; the Jackson Laboratory, strain

#014650], which contained a tet operator (tetO) upstream of the human TARDBP gene with a mutated nuclear localization sequence (tetO–hTDP-43–ΔNLS) leading to expression of cytoplasmic hTDP-43 (18). In double transgenic mice (referred to as ΔNLS mice), DOX can bind to tTA to prevent tetO-mediated transgene expression. DOX-supplemented chow (200 mg/kg; VWR, 89067-462) was provided to breeding pairs and offspring until weaning [postnatal day 21 (P21)] to prevent expression of transgene during embryonic and postnatal development. Thereafter, mice were maintained on standard laboratory chow (Purina 5053) to allow the induction of transgene expression. Because the parent tetO–hTDP-43–ΔNLS strain was on a B6/C3 hybrid background, we backcrossed this line onto the C57Bl/6J background (the Jackson Laboratory, strain #000664) for five generations.

Aldehyde dehydrogenase 1 family, member L1 (Aldh1l1)–Cre transgenic mice [B6;FVB-Tg(Aldh1l1-cre)JD1884Htz/J] were obtained from the Jackson Laboratory (strain #023748) and backcrossed onto the C57Bl/6J background. Aldh1l1-Cre mice express Cre recombinase downstream of the astrocytic Aldh1l1 promoter. Homozygous Aldh1l1-Cre mice were crossed with transgenic mice null for the chemokine receptor CXCR3 (B6.129P2-Cxcr3tm1Dgen/J; the Jackson Laboratory, strain #005796) to create Aldh1l1-Cre/Cxcr3-WT and Aldh1l1-Cre/Cxcr3-KO male mice. Hippocampal tissue from transgenic mice expressing mutant human tau-P301S [B6;C3-Tg(Prnp-MAPT*P301S)PS19Vle/J; the Jackson Laboratory, stock #008169] was used for gene expression comparisons.

AAV preparation

WT and mutant forms of hTDP-43 were cloned into plasmids for pAAV-mediated, astrocyte-specific expression in two stages. First, the truncated human astrocyte-specific promoter hGfaABC1D (51) was digested from pAAV-GFAP–enhanced green fluorescent protein (eGFP) (donated by B. Roth; Addgene, plasmid #50473; RRID #Addgene_50,473) and cloned into pAAV-EF1a-DIO-hM4D(Gi)-mCherry (donated by B. Roth; Addgene, plasmid #50461; RRID #Addgene_5046) in place of the elongation factor 1-α (EF1a) promoter using Anza 28 Mlu I and Anza 14 Sal I (Thermo Fisher Scientific). The inverted hM4D(Gi)-mCherry coding sequence in the resulting vector was replaced with inverted human WT or NLS1 TDP-43 coding sequences (117) by PCR amplification. Primers were designed to contain Nhe I and Sgs I restriction sites 5′ and 3′ to the TDP-43 coding sequence, respectively (Nhe I primer, 5′-TGT CGC TAG CGC CAC CAT GTC TGA ATA TAT TCG G-3′; Sgs I primer, 5′-AAG GCG CGC CCT ACA TTC CCC AGC CAG AAG-3′). Amplicons were digested and gel-purified before ligation into similarly prepared pAAV-GfaABC1D-DIO backbone. The pcDNA3.2 TDP-43 yellow fluorescent protein vectors were donated by A. Gitler (Addgene, plasmids # 84911 and 84912; RRID Addgene_84911 and Addgene_84912).

Mouse CXCR3 with a C-terminal hemagglutinin tag was targeted to neuronal presynaptic terminals using the neurexin-1α targeting sequence, as described (84). A gBlock gene fragment (Integrated DNA Technologies) encoding mCherry-T2A-CXCR3-2HA–neurexin-1α (axon targeting sequence) was designed following sequences made available by S. Sternson (Addgene, plasmid #52523; RRID #Addgene_52523), synthesized, and cloned into an AAV-hSyn1 expression vector (donated by B. Roth; Addgene, plasmid #50458; RRID #Addgene_50458) using Sal I and Eco RI restriction digest to generate pAAV-hSyn1:mCherry-T2A-CXCR3-2HA–neurexin-1α. NEB 5-alpha cells (New England Biolabs) were transformed with pAAV constructs, and the integrity of inverted terminal repeats and expression-related elements in selected clones were confirmed by sequencing and restriction digests. pAAV2/PHP.eB or pAAV2/DJ particles were produced by the Stanford University Neuroscience Gene Vector and Virus Core or the University of Pennsylvania Vector Core. PHP.eB capsid vectors were provided courtesy of V. Gradinaru and B. Deverman at the California Institute of Technology. PHP capsids are a modification of AAV9 provided by the University of Pennsylvania (52).

Surgery and AAV microinjections

Mice were anesthetized with sterile Avertin (2,2,2-tribromoethanol, 400 to 500 mg/kg body weight; Acros Organics), and the hair was removed from the surgical area. Mice were secured in a stereotaxic frame (Kopf Instruments), and 1-mm-diameter openings were made bilaterally in the skull using a mounted drill (Kopf Instruments). Meloxicam (2 mg/kg) was injected subcutaneously, and bupivacaine (1 mg/kg) was applied topically to relieve pain. Stereotaxic coordinates used for hippocampal injections were (from bregma) anterior/posterior: −2.1, medial/lateral: ±1.7, and dorsoventral: −2.0 (for mice under 23 g of body weight) or −2.1 (for mice over 23 g of body weight). A blunt 32-gauge, 1.27 cm-long needle attached to a 5-μl Hamilton syringe was mounted to the stereotaxic frame and controlled using a Micro 4 Microsyringe Pump (World Precision Instruments) to infuse 0.5 μl of AAV2/PHP.eB-hGfaABC1D-DIO–hTDP-43–WT (1.2×10^{13} particles/μl), AAV2/PHP.eB-hGfaABC1D-DIO–hTDP-43–ΔNLS (1.3×10^{13} particles/μl), or AAV2/PHP.eB-hGfaABC1D-DIO-hM4Di-mCherry (3.15×10^{12} particles/μl) at right and left injection sites at a rate of 0.1 μl/min, after which the needle was left in place for an additional 5 min. After needle withdrawal, the surgical site was sealed with Vetbond tissue adhesive (3M). Mice were monitored under a heating lamp until fully recovered and returned to their home cage.

Behavioral testing

Experimental groups were distributed randomly across home cages and consisted of age-matched littermates of both sexes. Experimenters were blinded to genotypes and treatment conditions, and mice were tested in random order. Before most behavioral testing, except for the elevated plus maze, all mice were handled for approximately 2 min/day for 7 days. Mice that were injured or in poor health, independent of genotype, were excluded from behavioral testing. Tests were performed under white light, unless otherwise noted. For all test days, mice were acclimated to the testing room for 1 hours before testing. Sample sizes were chosen on the basis of our previously published work (39) and studies by other groups (42).

Elevated plus maze

The plus-shaped maze consisted of two enclosed arms and two open arms elevated 60 to 70 cm above the ground. Furthermore, tape was attached to the ends of the open arms (5 cm from the end of the arm) to limit falls. After 1 hour of habituation, mice were placed at the center of the maze facing an open arm. Mice could freely explore the four arms for 5 min. Time and distance traveled in each arm and center area were video recorded and tracked using EthoVision XT video tracking software (Noldus Information

Technology Inc., Leesburg, VA). The apparatus was cleaned with 70% alcohol between mice.

Open field test

Mice were placed in the center of a clear plastic chamber (41 cm by 41 cm by 30 cm) with two 16 by 16 photobeam arrays detecting horizontal and vertical movements. To measure context-dependent habituation in the open field, the chambers were surrounded by distinct cues that were maintained across test days. Mice were acclimated to the chamber in 2×5–min trials with a 3-hour intertrial interval and assessed in the same chambers 1 and 14 days after habituation. Light in the room was set to 75% red light to limit the anxiolytic effect of 100% white light. Total exploration, rearing, and percent time spent in the center of the arena were measured with an automated Flex-Field/Open Field Photobeam Activity System (San Diego Instruments, San Diego, CA). The apparatus was cleaned with 70% alcohol between mice.

Rotarod

Mice were placed on the Rotarod (Rotamex-5, 0254-2002L) that was suspended 25.5 cm from a soft surface. The speed of rotation was either held constant at 12 rpm or increased from 4 to 40 rpm gradually at an acceleration rate of 0.3 rpm/s. Mice were tested on the rod in three trials with approximately 30-min intertrial intervals. The latency to fall off the rod was recorded and reported as the average of three trials. Equipment was cleaned with 70% ethanol between trials, and the light in the room was set to red light.

Morris water maze

The maze consisted of a 122-cm-diameter pool filled with water ($20° \pm 2°C$) made opaque with nontoxic white tempera paint (Colorations powder tempera paint). Spatial cues were set up around the pool before testing. All mice underwent one session of three to four pretraining trials in which they swam in a rectangular channel (15 cm by 122 cm) with a square platform (14 cm by 14 cm) hidden 0.5 cm below the water surface in the middle of the channel. If a mouse did not reach the platform within 10 s, then it was guided onto the platform by the experimenter and remained on the platform for 10 s before it was returned to its cage. One to 3 days following pretraining, mice underwent hidden platform training in the circular water maze.

For hidden platform training, the platform was submerged 1.5 cm below the surface. All mice underwent one session of four trials for three to five consecutive training days. For each trial, the platform location remained the same, but the mice were dropped in four different locations. The maximum time allowed per trial was 60 s. If a mouse did not find or mount the platform, then it was guided to the platform by the experimenter. All mice were allowed to sit on the platform for 10 s after each training trial.

Probe trials were performed 24 and 72 hours after the last hidden platform-training day. For probe trials, the platform was removed, and mice were allowed to swim for up to 60 s per trial. The drop location for the probe trials was 180° from the platform location used during hidden platform training. After 60 s, mice were guided to the platform location before removal from the pool and returned to its cage.

If the mice had any problems in learning where the platform is located, we performed a cued platform training 24 hours after probe testing. All mice underwent one session of four trials of the cued platform training. The cued (visible) platform training was performed using a different platform location and a clearly visible cue (a colorful 15-cm pole on top of the platform). All behavior

was recorded and analyzed with an EthoVision XT video tracking system (Noldus). Escape latencies, distance traveled, swim paths, swim speeds, platform crossings, and proximity to the platform were recorded automatically for subsequent analysis.

Novel object recognition test

Mice were habituated to the testing chamber (40 cm by 40 cm) for 15 min. A day after habituation, mice were exposed to two identical objects in the same chamber and allowed to explore freely for 10 min once per day for two consecutive days. The next day, mice were presented with one object used during training and one unfamiliar (novel) object of a different shape and texture in the same chamber, and the mice were allowed to explore for 15 min during a test trial. The objects used for training and testing were assigned randomly to each mouse to avoid object bias, and which of the familiar objects was replaced with an unfamiliar object was varied randomly between mice to control for location bias. Chamber and objects were cleaned with Clidox-S (Pharmacal; 1:18:1 dilution) after each mouse. Behavior was recorded and analyzed with an EthoVision XT video tracking system (Noldus) the time that the mice spent next to each object were scored.

Social interaction test

Mice were allowed to freely explore a three-chamber arena (side chambers were 22.86 cm by 42.2 cm; middle chamber was 21.59 cm by 42.2 cm) with two empty inverted wire cups (8.5 cm in diameter) in each side chamber. Chambers were divided by clear plexiglass dividers, each with a half-circular opening at the bottom to serve as a free passageway between chambers. After 10 min of exploration by a test mouse, an unfamiliar mouse of the same sex as the test mouse was placed under one inverted wire cup and the other wire cup was left empty. The test mouse was allowed to freely explore the three-chamber arena for another 10 min to explore the unfamiliar partner. Each unfamiliar mouse used for testing was assigned randomly to each side to avoid location bias. Chambers and wire cups were cleaned with 70% ethanol after each mouse. Behavior was recorded and analyzed with the EthoVision XT video tracking system (Noldus). The total time that the test mouse spent next to each inverted wire cup with a mouse or empty wire cup was scored. The light in the room was set to red light.

Marble-burying test

Mice were placed in large cages (12 cm by 12 cm by 7.25 cm) covered with mouse bedding material to a depth of 5 cm. During each trial, 20 standard glass black marbles were gently placed on the surface of the bedding in a grid pattern. A mouse was placed in the center of the cage and allowed to explore for 30 min. A marble was scored as buried when it was at least three-fourth covered with bedding. The light in the room was set to red light. Between trials, the bedding was changed, and the cages and marbles were cleaned with 70% ethanol.

Nestlet-shredding test

Mice were single-housed with one cotton fiber nestlet (5 cm by 5 cm, 5 mm in thickness, ~2.5 g each) for 60 to 90 min. Nestlets were weighed before putting them in the cages. After returning the mouse to its home cage, whole nestlet pieces (not the shredded nestlet) were removed, dried overnight, and weighed.

Grooming test

Mice were sprayed three times with a light water mist on the back and neck areas. The mice were placed in large cages (12 cm by 12 cm by 7.25 cm) with no bedding. Behavior was recorded with the EthoVision XT video tracking system (Noldus) for 10 min. Cages

were cleaned with 70% ethanol after each mouse. The amount of time spent grooming the head and the rest of the body was recorded and analyzed. The light in the room was set to red light.

Pole test

A vertical metal pole (1 cm in diameter and 50 cm in height) with a heavy metal base was placed in the center of a clean cage covered with bedding. Individual mice were placed on the upper portion of the pole facing the ceiling for three trials. The amount of time spent turning at the top of the pole and climbing down is video-recorded (EthoVision XT video tracking system, Noldus) and quantified. The apparatus was cleaned with 70% ethanol after each mouse. The light in the room was set to red light.

Wire hanging test

Individual mice were placed on top of a 2-mm-thick metal cloth hanger that is securely attached 40 cm above the home cage containing extra padding. For three consecutive days, the mouse was allowed to grasp the wire with the two forepaws for a maximum of 300 s for three trials. The latency of the mouse to full was recorded and quantified. The apparatus was cleaned with 70% ethanol after each mouse. The light in the room was set to red light.

Cell culture experiments

Primary astrocyte cultures

All cultures were maintained at 37°C in a humidified 5% CO_2-containing atmosphere. Cortices and/or hippocampi from WT (C57Bl/6J; the Jackson Laboratory, strain #000664), Aldh1l1-Cre [B6;FVB-Tg(Aldh1l1-cre)JD1884Htz/J, the Jackson Laboratory, strain #023748] or hemizygous double transgenic ΔNLS pups of mixed sex at P1 to P3 were dissected in cold phosphate-buffered saline (PBS) to remove meninges and dissociated by manual trituration with a P1000 pipette in 1 ml of fresh culture medium consisting of high-glucose Dulbecco's minimum essential medium (DMEM; Corning), 20% heat-inactivated fetal bovine serum (FBS; VWR, #89510-188), 1× GlutaMAX (Thermo Fisher Scientific, #35050061), and 1 mM sodium pyruvate (Thermo Fisher Scientific). In some experiments, culture medium for isolated astrocytes derived from double transgenic TDP-43–ΔNLS mice contained tetracycline-depleted FBS (VWR, #97065-310) that was heat-inactivated for 30 min at 56°C in a water bath. To prevent transgene expression, some cultures were treated with DOX hyclate (2 μg/μl; MilliporeSigma, #D9891). Cell suspensions were diluted to 10 ml with medium, filtered through a 70-μm cell strainer (VWR), centrifuged at 300g for 5 min at 22°C, resuspended with culture medium, and plated into cell culture dishes precoated with poly-ᴅ-lysine (75 to 150 kDa; 0.01% in water, filtered; Sigma-Aldrich, #P6407, or MP Biomedicals, #0215017580). At DIV (days in vitro) 4 to 5, the cells were washed to remove debris and given fresh medium.

WT and double transgenic astrocyte cultures were determined to contain 98.8 ± 0.4% (SE) of astrocytes and 1.2 ± 0.4% (SE) of microglia, based on immunolabeling for GFAP, Iba1, NeuN, and DAPI. These analyses were performed using a Nikon Eclipse Ti-S microscope with a Nikon PlanFluor 10× objective and NIS-Elements BR v5.02.01 acquisition software.

In double transgenic TDP-43–ΔNLS cultures without DOX treatment, hTDP-43 expression was detected in 47.8 ± 4.7% (SE) of astrocytes, based on immunolabeling for hTDP-43 and the astrocyte marker GFAP. For these analyses, a stringent lower cutoff was determined using mean signal intensity in parallel cultures with DOX treatment, which accounted for nonspecific

immunoreactivity and background fluorescence. For analyses of hTDP-43 distribution in cultures, images were captured with an LSM 880 confocal microscope (Zeiss) equipped with a 63× objective (Zeiss) and Zen Black v2.3 SP1 FP3 acquisition software (Zeiss). Images were processed in Fiji v2.1.0/1.53c by subtracting the average background fluorescence and analyzing individual cells that had DAPI-positive nuclei and GFAP-positive cell bodies for levels of nuclear and extranuclear hTDP-43 immunoreactivity, respectively.

Primary neuronal cultures

Cortical and hippocampal neurons from P0 to P1 WT or KO mouse pups (B6.129P2-Cxcr3tm1Dgen/J; the Jackson Laboratory, strain #005796) were obtained as described previously (118), with minor modifications. Briefly, papain-dissociated cells were filtered through a 0.4-μm cell strainer (Corning, #431750) to enrich for neurons, centrifuged at 500g for 5 min to eliminate small debris, and suspended in complete primary neuronal medium consisting of B-27 Plus Neuronal Culture system (Thermo Fisher Scientific, #A3653401) and 1× GlutaMAX (Thermo Fisher Scientific, #35050061) without antibiotics. Cells were seeded at 50,000 to 150,000 live cells/cm^2 into plates coated with poly-ᴅ-lysine (0.01%, w/v; Sigma-Aldrich, P6407). Medium was fully exchanged 1 day after plating (DIV 1) with subsequent half-medium exchanges every 3 to 4 days.

Chemokine treatments in primary neurons

For immunostaining, primary WT neurons were cultured on poly-ᴅ-lysine–coated black walled μCLEAR 96-well plates (Greiner Bio-One, #655090). For recording neuronal activity, primary WT neurons were plated onto poly-ᴅ-lysine coated 48-well CytoView MEA plates (Axion BioSystems) as described above. Neurons were transduced at DIV 8 with 2 × 10^8 AAV2/DJ-hSyn1:mCherry-T2A-Cxcr3-2HA–neurexin-1a particles per well. Starting at DIV 9, neuronal activity was recorded for 15 to 30 min daily before and after treatment with recombinant CXCL11 (200 nM; BioLegend, #573606) using the Maestro Pro MEA System (Axion BioSystems). Neuronal firing rates were analyzed using Neural Metric software (Axion BioSystems).

For RT-qPCR or Western blotting, primary WT neurons were cultured on Tissue Culture (TC)-treated 24-well plates (Greiner Bio-One, #662160). For chronic treatment with chemokines, neurons were treated with 200 nM CXCL11 (BioLegend, #573606) or PBS vehicle (VWR, #76018-870) starting at DIV 4 with reapplication at 2× concentrations during half-volume feedings at DIV 7 and 11. At DIV 14, neurons were fixed for immunostaining or harvested for RT-qPCR, as described in the "Immunocytochemistry" or "Microfluidic qPCR" section. To confirm the effects of chemokine stimulation on intracellular signaling, mouse Neuro-2a cells [American Type Culture Collection (ATCC), #CCL-131] maintained in high-glucose DMEM (Corning), 10% heat-inactivated FBS (VWR, #89510-188), 1× GlutaMAX (Thermo Fisher Scientific, #35050061), and 1 mM sodium pyruvate (Thermo Fisher Scientific) were transfected with AAV2/DJ-hSyn1:mCherry-T2A-Cxcr3-2HA–neurexin-1α using Lipofectamine 3000. To assess the chronic effects of chemokine stimulation on synaptic markers, neurons were treated at DIV 10 with 200 nM recombinant mouse CXCL11 or PBS (vehicle) for 72 hours before fixing with 4% paraformaldehyde (PFA) in 4% sucrose in PBS and immunostaining at DIV 13. For measuring G_i-coupled phosphosignaling, after overnight starvation, Neuro2a were acutely treated

with PBS (vehicle) or CXCL11 for 0, 2, or 10 min before harvesting as described in the "Western blotting" section.

Primary astrocytic-neuronal cocultures

Cortical and/or hippocampal astrocytes at P1 to P3 were cultured as described above. Before seeding neurons, near-confluent monolayers (typically 5 to 8 days after plating) were briefly rinsed of serum-containing medium. Neuronal suspensions were obtained from cortical and hippocampal tissue of P0 mouse pups as described above and seeded at 50,000 live cells per MEA on top of existing rinsed astrocyte monolayers in neuronal medium, as described above.

Astrocytes were plated onto poly-D-lysine–coated 48-well Cyto-View MEA plates (Axion BioSystems), as described above. After 6 to 8 days, cells were washed and transduced with 2 μl per well of AAV2/PHP.eB-$hGfaABC_1D$-DIO–TDP-43-WT (1.2×10^{13} particles/μl) or AAV2/PHP.eB-$hGfaABC_1D$-DIO–TDP-43–ΔNLS (1.3×10^{13} particles/μl). After 3 to 5 days, primary neurons were isolated and seeded on top of the transduced astrocytes as described above. Neural activity was recorded for 15 to 30 min daily between neuronal DIV 8 and 18 using the Maestro Pro MEA System (Axion BioSystems), and firing rates were analyzed using Neural Metric software (Axion Bio-Systems). Some wells received the CXCR3 antagonist SCH 546738 (12 nM; MedChemExpress, #HY-10017).

Slice electrophysiology
Slice preparation

Mice were deeply anesthetized with 5% isoflurane before being cardially perfused with ice-cold and oxygenated (95% O_2/5% CO_2) sucrose cutting solution. Sucrose cutting solution contained 87 mM NaCl, 75 mM sucrose, 2.5 mM KCl, 1.25 mM NaH_2PO_4, 0.5 mM $CaCl_2$, 25 mM $NaHCO_3$, 1.3 mM ascorbic acid, and 10 mM D-glucose. The mice were quickly decapitated, and the brain was extracted in ice-cold sucrose cutting solution. Coronal slices (350 μm in thickness) were made on a vibrating blade microtome (Leica, VT1200s) while submerged in ice-cold and oxygenated sucrose cutting buffer. Slices were transferred to a heated (~35°C) incubation chamber containing artificial cerebral spinal fluid (ACSF), which consisted of 124 mM NaCl, 2.5 mM KCl, 1.5 mM $MgSO_4$, 1.25 mM NaH_2PO_4, 2.5 mM $CaCl_2$, and 26 mM $NaHCO_3$. After approximately 30 min, the incubation chamber was allowed to equilibrate to room temperature for at least an additional 30 min.

Field potential recordings

For recordings, slices were transferred to a stage-mounted holding chamber on an upright BX51W1 microscope (Olympus). The chamber was superfused (2 to 3 ml/min) with oxygenated (95% O_2/5% CO_2) and heated (~35°C) ACSF. Recordings were obtained using a Multiclamp 200B amplifier (Molecular Devices) and filtered at 2 kHz, digitized at 10 kHz, and acquired with Clampex 10.7 (Molecular Devices). Micropipettes were made with borosilicate glass pulled to a resistance of 3.5 to 5.5 megohm on a Flaming/Brown P-1000 micropipette puller (Sutter Instruments) and filled with the same ACSF. These were placed in the stratum radiatum of CA1, and a concentric bipolar stimulating electrode was placed within the same layer, upstream of the Schaffer collaterals. Care was taken to keep the recording pipette and stimulating electrode as far apart as possible (at least 200 μm) to help isolate the stimulus artifact, the fiber volley, and the field potential. For the stimulus intensity/field potential slope relationship, once a minimal current to

reliably evoke a fiber volley and field potential was established, the stimulus current was systematically increased, and the subsequent fiber volley and field potential were recorded. For paired-pulse ratio recordings, stimulus intensity was set to approximately half-maximal intensity. Recordings were analyzed using custom code in MATLAB (MathWorks), Excel (Microsoft), or Prism (GraphPad).

VSV production, purification, and quantification

Human 293T cells (ATCC, #CRL-3216) were plated at 1×10^6 cells per well in six-well plates. The following day, the cells were rinsed with serum-free medium and transfected with a mixture of plasmids encoding the rVSV antigenome, rVSV-ΔG-Luciferase (500 ng; Kerafast, #EH1007), and the rescue plasmids pCAG-VSVP (Addgene, plasmid #64088), pCAG-VSVN (Addgene, plasmid #64087), pCAG-VSVM (Addgene, plasmid #64086), pCAG-VSVL (Addgene, plasmid #64085), pCAG-VSVG (Addgene, plasmid #64084), and pCAG-T7pol (Addgene, #59926). Lipofectamine 3000 (Thermo Fisher Scientific, #L3000001) was used for transfection according to the manufacturer's instructions. After 48 hours, the supernatant was collected, filtered through a 0.4-μm filter, and used to infect VSV-G–expressing cells for amplification. To amplify rescued rVSV-ΔG-Luciferase, 5×10^6 293T cells were plated in a 10-cm dish with 10 ml of growth medium, or 1.2×10^7 293T cells were plated in a 15-cm dish. The cells were transfected with 5 μg (in a 10-cm dish) or 12.5 μg (in a 15-cm dish) of pCMV-VSV-G expression plasmid (Addgene, plasmid #8454) using Lipofectamine 3000. The following day, the transfected cells were infected with the rescued virus, and 24 to 48 hours later, the supernatant was collected, centrifuged at 350g to clarify, and filtered through a 0.22-μm filter. VSV stock titer was quantified by serial dilution, followed by infection. Briefly, 293T cells were plated at 2×10^5 cells per well in 24-well plates. The following day, cells were rinsed with serum-free medium and infected with serially diluted VSV. Medium was changed 2 hours after infection, and the cells were fixed and immunostained 48 hours after infection to detect firefly luciferase (Abcam, #ab181640; RRID #AB_2889835).

VSV and adenovirus infections

Primary astrocytes from NTG and double transgenic ΔNLS mice were transfected with 0.66 μg of low–molecular weight poly(I:C) (InvivoGen, #tlrl-picw) per ml of culture medium at DIV 8 using Lipofectamine 3000 5 hours before infection with VSV at 100 multiplicity of infection (MOI) or with adenovirus-eGFP (Ad5CMV-eGFP, lot #ad3586, Viral Vector Core Facility, Carver College of Medicine, University of Iowa) at indicated MOIs (see figures). A change of medium was made 2 hours after viral infections, and the cells were collected 24 hours after infection. VSV levels were measured by RT-qPCR. eGFP fluorescence was analyzed after cultures were fixed with 4% PFA in PBS and stained with DAPI. Fluorescence intensity (integrated density), area, and percent of total area were extracted using Fiji. Data are represented as eGFP normalized to the total DAPI-positive area and percentage of DAPI-positive area per condition.

HSV-1 infections

HSV-1 H129-eGFP strain was generously provided by L. Enquist (Princeton University, Princeton, NJ). Viral stocks were grown on

human Vero E6 cells (ATCC, CRL-1586) maintained in DMEM with 10% FBS. Standard plaque assays were performed to titer HSV-1 H129-eGFP stocks and quantify viral load in conditioned medium from infected primary astrocytes. Briefly, stocks or medium samples were serially diluted in DMEM supplemented with 2% FBS and used to infect Vero cells. After 3 hours, cells were washed three times with PBS and further incubated in DMEM with 2% FBS, antibiotics, and 1.5% methylcellulose (37°C). After 48 hours, cultures were fixed with 4% PFA in PBS and counterstained with Hoechst 33342 (Thermo Fisher Scientific). Fluorescent signal was used to detect plaques of infected cells and quantify viral titers. Cell culture plates were imaged on a BX-X710 microscope (Keyence) with a 20× objective (Nikon). Images were stitched with BZ-X Analyzer software (Keyence) and used to count plaques.

Immunocytochemistry

All immunostaining steps were performed at ambient temperature unless specified otherwise. Briefly, cells were fixed with 4% PFA and 4% sucrose in PBS for 10 min, rinsed four times with PBS (Corning) with 0.01% Triton X-100, and blocked and permeabilized in 5% normal goat serum (Jackson ImmunoResearch) or 5% normal donkey serum (Jackson ImmunoResearch) in 0.2 to 0.3% Triton X-100 in PBS for 1 hour. Cells were incubated overnight at 4°C with the following primary antibodies diluted in 1% bovine serum albumin (BSA), 2% normal donkey serum, or 2% normal goat serum in 0.2 to 0.3% Triton X-100 in PBS: mouse anti–PSD-95 (1:1000; Antibodies Incorporated, #75-028; RRID #AB_2292909), guinea pig anti–synaptophysin 1 (1:750; Synaptic Systems, #101004; RRID #AB_1210382), rabbit anti-bassoon (1:1000; Synaptic System, #141003; RRID #AB_887697), rabbit anti–red fluorescent protein (1:500; Abcam, #ab34771; RRID # AB_777699), human-specific mouse anti–TDP-43 (1:500; clone 6H6E12; ProteinTech, # 60019-2-Ig; RRID #AB_2200520), or goat anti-GFAP (1:500; Abcam, #ab53554; RRID #AB_880202). Cells were rinsed four times with PBS with 0.01% Triton X-100 and incubated for 1 hours with the following Alexa Fluor–conjugated secondary antibodies diluted in 1% BSA, 2% normal donkey serum, or 2% normal goat serum and 0.2 to 0.3% Triton X-100 in PBS (1:500; Thermo Fisher Scientific, #A11073, A31571, and A31572; RRID # AB_2534117, AB_162542, and AB_162543). Cells were rinsed twice with PBS with 0.01% Triton X-100 and twice with PBS before imaging.

Immunohistochemistry

Postmortem human brain tissue blocks or sections from nondemented controls, AD, or behavioral variant frontotemporal dementia (bvFTD) cases were obtained from the Neurodegenerative Disease Brain Bank at University of California, San Francisco (San Francisco, CA) and the Banner Sun Health Research Institute Brain and Body Donation Program of Sun City, Arizona. Case details are listed in table S1. Formalin-fixed tissue blocks were rinsed in PBS and incubated in 30% sucrose for 3 to 5 days at 4°C before sectioning.

Mice were anesthetized with Avertin (2,2,2-tribromoethanol, 400 to 600 mg/kg body weight; Acros Organics) and transcardially perfused for 2.5 min with 0.9% saline before hemibrains were removed and stored in fixative (4% PFA in PBS) overnight at 4°C on a rocking platform. Hemibrains were subsequently incubated

in cryoprotectant (30% sucrose in PBS) for at least 48 hours before sectioning.

Human and mouse brain tissue was sectioned (30-μm-thick sections) using a SM2010 R sliding microtome (Leica) equipped with a BFS-3MP freezing stage and cooling unit (Physitemp, Clifton, NJ). Free-floating sections were collected into cryopreservative (30% ethylene glycol and 30% glycerol in PBS) for long-term storage at −20°C.

Human tissue was immunolabeled by rinsing sections in PBS and permeabilizing overnight in PBS containing 0.5% Triton X-100 (PBS-T). Antigen retrieval was performed for 15 min in hot 0.1 M citrate buffer at pH 6.0, followed by incubation for 15 min with 3% hydrogen peroxide and 10% methanol in PBS. Sections were blocked for 2 hours in 10% normal donkey serum (Jackson ImmunoResearch) and 2% nonfat dry milk and incubated overnight on a rocking platform with primary antibodies in 3% normal donkey serum. To minimize autofluorescence, sections were incubated for 20 min with 0.2-μm-filtered 0.3% Sudan Black B (Acros Organics) in 70% ethanol and then incubated with secondary antibodies in 3% normal donkey serum for 2 hours. The following primary antibodies were used for human tissue: pan-specific rabbit anti–TDP-43 (1:500; ProteinTech, #10782-2-AP; RRID #AB_615042), mouse anti-GFAP (1:500; Millipore, #MAB3402B; RRID #AB_10917109), mouse anti-Aldh1L1, clone N103/39 (1:1000; Millipore, #MABN495; RRID #AB_2687399), and Alexa Fluor–conjugated secondary antibodies (1:250; Thermo Fisher Scientific; listed below).

Double or triple immunolabeling of free-floating mouse sections was performed with minor modifications depending on the antibodies used. All steps were performed at ambient temperature unless specified. Cryopreserved sections were rinsed in PBS, permeabilized for 30 min or longer in PBS-T, blocked with 10% normal donkey or goat serum (Jackson ImmunoResearch) in PBS-T for 1 to 2 hours, incubated in primary antibodies in 3% serum in PBS-T for up to 48 hours at 4°C, and rinsed with PBS-T. Sections were protected from light in all subsequent steps. Tissue was incubated with fluorescent secondary antibodies in 3% serum in PBS-T for 2 hours, rinsed with PBS-T, mounted, and dried on Superfrost glass slides (VWR, #75799-266) before sealing #1.5 coverglass (VWR, #89239-734) with VECTASHIELD antifade medium containing DAPI (VWR, #101098-050). When necessary, Prolong Diamond Antifade Mounting Media (Thermo Fisher Scientific #P36970) replaced VECTASHIELD mounting medium to minimize quenching of Alexa Fluor 647–conjugated antibodies. Slides were allowed to set overnight before acquiring images.

Unless colabeled with an antibody requiring modified protocols described below, the following primary antibodies were used according to the general protocol: pan-specific rabbit anti–TDP-43 (1:1000; ProteinTech, #10782-2-AP; RRID #AB_615042), goat anti-CXCL10 (1:150; R&D Systems, #AF-466-NA; RRID #AB_2292487), rabbit anti-GFAP (1:1000; MilliporeSigma, #G9269; RRID #AB_477035), mouse biotin-anti-GFAP (1:1000; MilliporeSigma, #MAB3402B; RRID #AB_10917109), rabbit anti-NeuN (1:1000; MilliporeSigma, #ABN78; RRID #AB_10807945), mouse anti-NeuN (1:1000; MilliporeSigma, #MAB377; RRID #AB_2298772), rabbit anti-Iba1 (1:1000; Wako, #019-19741; RRID #AB_839504), and guinea pig anti–synaptophysin-1 (1:750; Synaptic Systems, #101004; RRID #AB_1210382). Following the permeabilization step, some antibodies required an antigen-retrieval step of

15 min in hot citrate buffer as described previously (*39*). These antibodies were mouse anti-viperin/*Cig5* (1:50; Abcam, #ab107359; RRID #AB_10888107), mouse anti–synaptotagmin-2 (1:200; Developmental Studies Hybridoma Bank, #znp-1-c), rabbit anti-CXCL9 (1:50; Abcam, #ab202961), rabbit anti-CXCR3 (1:200; ProteinTech, #26756-1-AP), rabbit anti–glutamine synthetase (1:250; Thermo Fisher Scientific, #701989; RRID #AB_2633045), and goat anti–PSD-95 (1:500; Abcam, #ab12093; RRID #AB_298846).

For labeling with certain mouse monoclonal antibodies, the serum in the blocking and antibody steps was replaced with reagents from the Mouse-on-Mouse Basic Immunodetection Kit following the vendor's instructions (Vector Laboratories, #BMK-2202). These antibodies were mouse anti-viperin/*Cig5*, mouse anti–synaptotagmin-2, human-specific mouse anti–TDP-43 (1:7000; clone 6H6E12; ProteinTech, #60019-2-Ig; RRID #AB_2200520), and mouse anti-gephyrin (1:200; Synaptic Systems, #147011; RRID #AB_887717). Note that antigen retrieval with hot citrate buffer eliminated labeling by the human-specific mouse anti–TDP-43 antibody. Alexa Fluor–conjugated secondary antibodies were obtained from Thermo Fisher Scientific (1:500; #A11055, A21202, A21206, A21432, A21435, A31570, A31571, and A31572; RRID #AB_2534102, AB_141607, AB_2535792, AB_141788, AB_2535856, AB_2536180, AB_162542, and AB_162543).

Microscopy and image analyses

Primary neurons were evaluated for synaptic content using a 40× objective on an ImageXpress Micro Confocal Au4tomated High-Content Analysis System (Molecular Devices) at the Weill Cornell Medicine Automated Optical Microscopy Core Facility. Briefly, four regions of interest (ROIs) were imaged per well, and images were processed to assess the number and total area of synaptophysin-1 or PSD-95–positive puncta using Fiji. Briefly, images of individual channels were background-subtracted and stringently thresholded to the brightest 5 to 10% of all pixels, and particles equal or larger than 1 µm in length were counted. The total area and number of thresholded puncta were measured for each image.

To measure astrocytic TDP-43 in human brain tissue, postmortem hippocampal tissue was immunostained with anti–TDP-43 and anti-GFAP antibodies and imaged on a BX-X710 microscope (Keyence) with a 40× objective (Nikon), and astrocytes were analyzed within the dentate gyrus and Cornu Ammonis regions. Tables S1 and S2 provide detailed information about the human cases and the numbers of cells analyzed per case. Image analysis was performed using Fiji. The patterns and intensities for TDP-43 and GFAP labeling were not consistently colocalized across cases and individual cells, indicating minimal bleed-through between channels.

Astrocytes were defined by drawing ROIs encompassing primary processes and cell soma with strong GFAP fluorescence together with overlapping or adjacent DAPI-positive nucleus. ROIs were extracted, and the intensity of nuclear TDP-43 immunoreactivity was measured for pixels within a DAPI-thresholded mask. The intensity of extranuclear TDP-43 immunoreactivity in GFAP-positive ROIs was measured for pixels in a GFAP-thresholded mask after eliminating the nuclear area defined by the DAPI mask. Intensities were corrected for background fluorescence in each image by subtracting the mean intensity of five circular ROIs drawn in areas that did not have GFAP, TDP-43, or DAPI labeling above background levels.

To evaluate cell-specific localization and intensity of protein expression in mouse brain sections, slides were imaged on a BX-X710 microscope (Keyence) with a 20× objective (Nikon) using the tiling function. Images were stitched with BZ-X Analyzer software (Keyence) and further processed for brightness and contrast using Fiji. To further evaluate cell localization of proteins in mouse brain sections, z-stacks of immunostained tissue were acquired on a Zeiss LSM 880 Confocal Laser Scanning Microscope with a 63× objective, and three-dimensional renderings of maximal projections were made using Imaris software (Oxford Instruments).

Localization of CXCR3 protein in neuronal cell bodies and synaptic compartments was evaluated using a Zeiss LSM 880 Confocal Laser Scanning Microscope. Images of the CA1 stratum radiatum region of the hippocampal formation were acquired using a 63× objective, 4× zoom, 16-line averaging, and a pixel dwell time of 5.3 µs. Filter and detector configurations were optimized using single-antibody controls, and each of the three channels was imaged sequentially to further minimize potential cross-bleed. Images were analyzed using Fiji to measure the number, area, and intensity of puncta that were immunoreactive for CXCR3 and NeuN, synaptophysin-1, synaptotagmin-2, PSD-95, or gephyrin.

Briefly, images of individual channels were background-subtracted, and noise was removed using the "despeckle" function. Images were stringently thresholded to the brightest 5 to 10% of pixels, and particles equal or larger than 1 µm in length were counted. The total area, mean size, and mean intensity of thresholded puncta were measured for each image. The fractional overlap of CXCR3 and each synaptic marker was measured from processed images as Mander's coefficient using the Just Another Colocalization Plugin (*119*). A total of 9 to 12 images from three to four mice were analyzed per genotype.

Western blotting

For cell cultures, wells were rinsed twice with ice-cold PBS before aspirating buffer and lysing directly with ice-cold 1× radioimmunoprecipitation assay (RIPA) buffer (Thermo Fisher Scientific, #89900) containing 1× cOmplete Protease Inhibitor Cocktail (MilliporeSigma, #11836153001) and 1% each of Phosphatase Inhibitor Cocktails 2 and 3 (MilliporeSigma, #P5726 and #P0044). Cells were scraped, collected in 1.5-ml Eppendorf tubes, sonicated on ice for 5 s at 10% power with a probe sonifier (Branson), centrifuged at 10,000*g* for 5 min at 4°C, and assayed for protein content using a detergent-compatible Bradford assay (Thermo Fisher Scientific, #23246).

For brain tissue, approximately 30 mg of mouse hippocampal tissue was dissected from flash-frozen forebrain in ice-cold PBS under a dissecting scope (AmScope) and refrozen on dry ice in 1.5-ml Eppendorf tubes. Frozen samples were thawed on ice for 1 to 2 min before adding 150 µl of ice-cold lysis buffer to each tube (RIPA with protease and phosphatase inhibitors). Samples were immediately homogenized with a Fisherbrand Bead Mill 24 (Thermo Fisher Scientific, #15-340-163) for 40 s at a speed setting of 5 in a prechilled adaptor tube rack. Samples were centrifuged at 1000*g* for 2 min at 4°C before sonication in an ice-chilled EpiSonic 2000 water bath (5-s on, 2-s off, 5-min total, amplitude of 40). RIPA-soluble extracts were clarified by centrifugation at 100,000*g* for 30 min at 4°C in a Beckman Ultracentrifuge, and protein content was measured using a detergent-compatible Bradford assay (Thermo Fisher Scientific).

For tissue and cell culture extracts, 30 or 20 μg RIPA-soluble lysates, respectively, were resolved on bis-tris SDS–polyacrylamide gel electrophoresis gels (Thermo Fisher Scientific) and transferred onto nitrocellulose membranes using an iBlot2 Western blotting system or a Mini Blot Module (Thermo Fisher Scientific). Membranes were blocked with 5% nonfat milk or 5% BSA (VWR, #97062-904) in tris-buffered saline (TBS) before probing overnight at 4°C with primary antibodies diluted in TBS containing 0.2% Tween 20 (TBS-Tw). Primary antibodies were raised against TDP-43 (1:2000; pan-specific rabbit anti–TDP-43; ProteinTech, #10782-2-AP; RRID #AB_615042; or 1:2000; human-specific mouse anti–TDP-43; ProteinTech, #60019-2-Ig; RRID #AB_2200520), β-actin (1:2000; rabbit; Sigma-Aldrich, #A2066; RRID #AB_476693), γ-tubulin (1:1250; mouse; Sigma-Aldrich, #T5326; RRID #AB_532292), NF-κB (1:1000; mouse anti-total NF-κB; Cell Signaling Technology, #6956; RRID #AB_10828935; or 1:1000; rabbit anti-phospho NF-κB-S536; Cell Signaling Technology, #3033; RRID #AB_331284), Akt (1:250; mouse anti-total Akt; Cell Signaling Technology, #2920; RRID #AB_1147620; or 1:2500; rabbit anti-phospho Akt (S473); Abcam, ab81283; RRID #AB_2224551), extracellular signal–regulated kinase 1/2 (ERK1/2) [1:1000; mouse anti-total ERK1/2; Cell Signaling Technology, #4696; RRID #AB_390780; or rabbit anti-phospho ERK1/2 (T202 and Y204); Cell Signaling Technology, #9101; RRID #AB_331646]. STAT3 (1:1000; mouse anti-total STAT3; Cell Signaling Technology, 9139S; RRID #AB_331757; or 1:1000; rabbit anti-phospho STAT3 (Y705); Cell Signaling Technology, 9145S; RRID #AB_2491009).

After overnight incubation in primary antibodies, all blots were rinsed with TBS-Tw and probed for 1 hour with IR Dye 680RD donkey anti-mouse (1:15,000; LI-COR, #926-68072; RRID #AB_2814912) and IR Dye 800CW donkey anti-rabbit (1:15,000; LI-COR, #926-32213; RRID #AB_621848) in TBS-Tw with 3% BSA. Blots were rinsed twice with TBS-Tw and once with TBS and dried for at least 20 min before scanning on the Odyssey CLx imaging system (LI-COR). Expression levels were quantified using LI-COR Image Studio software.

Enzyme-linked immunosorbent assays

Primary NTG and ΔNLS hippocampal astrocyte lysates and media were collected for protein analyses at DIV 11. Cultures were rinsed twice with ice-cold PBS, aspirated, and lysed in ice-cold lysis buffer consisting of Triton X-100 (0.5%), tris base (10 mM), EDTA (5 mM), deoxycholate (0.5%), NaCl (150 mM), 1× cOmplete Protease Inhibitor Cocktail (MilliporeSigma, #11836153001), and 1% each of Phosphatase Inhibitor Cocktails 2 and 3 (MilliporeSigma, #P5726 and #P0044). After 30 min in lysis buffer, cells were scraped, collected in 1.5-ml Eppendorf tubes, centrifuged at 14,000g for 5 min at 4°C, and assayed for protein content using a detergent-compatible Bradford assay (Thermo Fisher Scientific, #23246). Cell culture medium was collected and centrifuged at 500g for 5 min at 4°C before assessment.

CXCL10 concentrations in lysates and medium were determined using the IP-10 (CXCL10) Enzyme-linked immunosorbent assay (ELISA) kit (Thermo Fisher Scientific, #BMS6018), according to the manufacturer's instructions. IFN-γ concentrations in cell lysates were determined using IFN-γ ELISA kits from R&D Systems (#DY485-05) and Thermo Fisher Scientific (#88-8314-22), according to the manufacturers' instructions. For each kit, 3 μl of cell lysate were diluted in 97 μl of the provided Sample Diluent, and 50 μl of medium was diluted in 50 μl of the provided Sample Diluent. Concentrations were determined on the basis of standard curves, and values were corrected for the dilution factor.

Microfluidic qPCR

RNA was extracted using the RNeasy Mini Kit with on-column deoxyribonuclease treatment following manufacturer's instructions (QIAGEN, #74106 and #79256). Cultured primary cells were rinsed once with ice-cold PBS, scraped in freshly prepared extraction buffer, and frozen at −80°C until extracted. Saline-perfused, microdissected mouse brain tissue was frozen on dry ice and stored at −80°C until RNA extraction. Tissue was homogenized in fresh extraction buffer using a bead mill for 20 s at a speed setting of 5 in a prechilled adaptor tube rack.

Some NTG and ΔNLS hippocampal astrocyte cultures were treated at DIV 10 with dimethyl sulfoxide (DMSO) (0.01 to 0.2%), SN50 (10 μM; Cayman Chemicals, #17493), or Stattic (5 μM; MilliporeSigma, #S7947) for 24 hours before analyses.

The number of VSV viral copies was determined by RT-qPCR using PowerUp SYBR Green Master Mix (Thermo Fisher Scientific, #A25741) according to manufacturer's instructions. RT-qPCR was performed in a CFX96 Touch Real-Time PCR Detection System (Bio-Rad). All primer sequences are detailed in table S3.

Microfluidic RT-qPCR was performed similarly to previously described protocols (120). Briefly, cDNA was synthesized with the Protoscript First Strand Synthesis Kit (New England Biolabs, #E6300L) and preamplified for 14 cycles against a pool of primers (table S3) using PreAmp Grandmaster mix (TATAA Biocenter, Sweden, #TA05) before exonuclease I treatment (New England Biolabs, #M0293L). Preamplified cDNA was diluted at least fivefold with nuclease-free water and mixed with SsoFast EvaGreen with Low ROX (Bio-Rad, #1725211) and chip-specific DNA Sample Reagents before loading into primed Flex Six or 96.96 Dynamic Array chips (Fluidigm, #100-6308, BMK-M-96.96). Individual primers were mixed with DNA assay reagent (Fluidigm) and loaded into chip inlets. Chips were primed and loaded using an IFC Controller HX (Fluidigm) before measuring and analyzing amplification and melting curves on a BioMark HD System (Fluidigm). Cycle of quantification (Cq) values were thresholded equally for all inlets across each chip run and normalized to the average of reference genes (Actb and Gapdh for tissue samples and Actb and/or Tbp for cultured cells) before determining ΔΔCq and fold change relative to experimental control groups.

Statistical analyses

Statistical specifications are reported in the figures and corresponding figure legends. Replicates for the main figures are specified in table S4. Data are presented as means ± SEM. All statistical tests were performed using GraphPad Prism 8, except Fisher's exact test, which was performed using IBM SPSS Statistics for Windows, version 24.0. The criterion for data point exclusion was established during the design of the study and was set to values above or below two SDs from the group mean. Two-sided Student's t test was used to determine statistical significance between two groups. Welch's correction was used to account for unequal variances. Differences among multiple groups were assessed by one-way or two-way analysis of variance (ANOVA) or mixed-effects model, followed by Dunnett's or Bonferroni's multiple comparisons

post hoc tests, as specified in the legends. Null hypotheses were rejected at $P < 0.05$.

Supplementary Materials

This PDF file includes:
Figs. S1 to S7
Tables S1 to S4

Other Supplementary Material for this manuscript includes the following:
Extended Data for the Main Figures
Extended Data for the Supplementary Figures
Supplementary Uncropped Western Blot Images

View/request a protocol for this paper from *Bio-protocol*.

REFERENCES AND NOTES

1. T. Arai, M. Hasegawa, H. Akiyama, K. Ikeda, T. Nonaka, H. Mori, D. Mann, K. Tsuchiya, M. Yoshida, Y. Hashizume, T. Oda, TDP-43 is a component of ubiquitin-positive tau-negative inclusions in frontotemporal lobar degeneration and amyotrophic lateral sclerosis. *Biochem. Biophys. Res. Commun.* **351**, 602–611 (2006).
2. A. S. Chen-Plotkin, V. M. Lee, J. Q. Trojanowski, TAR DNA-binding protein 43 in neurodegenerative disease. *Nat. Rev. Neurol.* **6**, 211–220 (2010).
3. I. R. Mackenzie, R. Rademakers, M. Neumann, TDP-43 and FUS in amyotrophic lateral sclerosis and frontotemporal dementia. *Lancet Neurol.* **9**, 995–1007 (2010).
4. S. C. Ling, M. Polymenidou, D. W. Cleveland, Converging mechanisms in ALS and FTD: Disrupted RNA and protein homeostasis. *Neuron* **79**, 416–438 (2013).
5. C. Amador-Ortiz, W. L. Lin, Z. Ahmed, D. Personett, P. Davies, R. Duara, N. R. Graff-Radford, M. L. Hutton, D. W. Dickson, TDP-43 immunoreactivity in hippocampal sclerosis and Alzheimer's disease. *Ann. Neurol.* **61**, 435–445 (2007).
6. A. K. Walker, C. M. Daniels, J. E. Goldman, J. Q. Trojanowski, V. M. Lee, A. Messing, Astrocytic TDP-43 pathology in Alexander disease. *J. Neurosci.* **34**, 6448–6458 (2014).
7. H. K. Wang, Y. C. Lee, C. Y. Huang, P. C. Liliang, K. Lu, H. J. Chen, Y. C. Li, K. J. Tsai, Traumatic brain injury causes frontotemporal dementia and TDP-43 proteolysis. *Neuroscience* **300**, 94–103 (2015).
8. J. Gao, L. Wang, M. L. Huntley, G. Perry, X. Wang, Pathomechanisms of TDP-43 in neurodegeneration. *J. Neurochem.* **146**, 7–20 (2018).
9. K. Uryu, H. Nakashima-Yasuda, M. S. Forman, L. K. Kwong, C. M. Clark, M. Grossman, B. L. Miller, H. A. Kretzschmar, V. M. Lee, J. Q. Trojanowski, M. Neumann, Concomitant TAR-DNA-binding protein 43 pathology is present in Alzheimer disease and corticobasal degeneration but not in other tauopathies. *J. Neuropathol. Exp. Neurol.* **67**, 555–564 (2008).
10. Y. S. Davidson, S. Raby, P. G. Foulds, A. Robinson, J. C. Thompson, S. Sikkink, I. Yusuf, H. Amin, D. DuPlessis, C. Troakes, S. Al-Sarraj, C. Sloan, M. M. Esiri, V. P. Prasher, D. Allsop, D. Neary, S. M. Pickering-Brown, J. S. Snowden, D. M. Mann, TDP-43 pathological changes in early onset familial and sporadic Alzheimer's disease, late onset Alzheimer's disease and Down's syndrome: Association with age, hippocampal sclerosis and clinical phenotype. *Acta Neuropathol.* **122**, 703–713 (2011).
11. K. A. Josephs, M. E. Murray, J. L. Whitwell, J. E. Parisi, L. Petrucelli, C. R. Jack, R. C. Petersen, D. W. Dickson, Staging TDP-43 pathology in Alzheimer's disease. *Acta Neuropathol.* **127**, 441–450 (2014).
12. S. Nag, L. Yu, A. W. Capuano, R. S. Wilson, S. E. Leurgans, D. A. Bennett, J. A. Schneider, Hippocampal sclerosis and TDP-43 pathology in aging and Alzheimer disease. *Ann. Neurol.* **77**, 942–952 (2015).
13. M. Buciuc, N. Tosakulwong, M. M. Machulda, J. L. Whitwell, S. D. Weigand, M. E. Murray, R. R. Reichard, J. E. Parisi, D. W. Dickson, B. F. Boeve, D. S. Knopman, R. C. Petersen, K. A. Josephs, TAR DNA-binding protein 43 is associated with rate of memory, functional and global cognitive decline in the decade prior to death. *J. Alzheimers Dis.* **80**, 683–693 (2021).
14. A. Ratti, E. Buratti, Physiological functions and pathobiology of TDP-43 and FUS/TLS proteins. *J. Neurochem.* **138**(Suppl. 1), 95–111 (2016).
15. F. B. Gao, S. Almeida, R. Lopez-Gonzalez, Dysregulated molecular pathways in amyotrophic lateral sclerosis-frontotemporal dementia spectrum disorder. *EMBO J.* **36**, 2931–2950 (2017).
16. C. C. Chou, Y. Zhang, M. E. Umoh, S. W. Vaughan, I. Lorenzini, F. Liu, M. Sayegh, P. G. Donlin-Asp, Y. H. Chen, D. M. Duong, N. T. Seyfried, M. A. Powers, T. Kukar, C. M. Hales, M. Gearing, N. J. Cairns, K. B. Boylan, D. W. Dickson, R. Rademakers, Y. J. Zhang, L. Petrucelli, R. Sattler,

D. C. Zarnescu, J. D. Glass, W. Rossoll, TDP-43 pathology disrupts nuclear pore complexes and nucleocytoplasmic transport in ALS/FTD. *Nat. Neurosci.* **21**, 228–239 (2018).
17. M. S. Fernandopulle, J. Lippincott-Schwartz, M. E. Ward, RNA transport and local translation in neurodevelopmental and neurodegenerative disease. *Nat. Neurosci.* **24**, 622–632 (2021).
18. L. M. Igaz, L. K. Kwong, E. B. Lee, A. Chen-Plotkin, E. Swanson, T. Unger, J. Malunda, Y. Xu, M. J. Winton, J. Q. Trojanowski, V. M. Lee, Dysregulation of the ALS-associated gene TDP-43 leads to neuronal death and degeneration in mice. *J. Clin. Invest.* **121**, 726–738 (2011).
19. L. S. Wu, W. C. Cheng, C. K. Shen, Targeted depletion of TDP-43 expression in the spinal cord motor neurons leads to the development of amyotrophic lateral sclerosis-like phenotypes in mice. *J. Biol. Chem.* **287**, 27335–27344 (2012).
20. Y. Iguchi, M. Katsuno, J. Niwa, S. Takagi, S. Ishigaki, K. Ikenaka, K. Kawai, H. Watanabe, K. Yamanaka, R. Takahashi, H. Misawa, S. Sasaki, F. Tanaka, G. Sobue, Loss of TDP-43 causes age-dependent progressive motor neuron degeneration. *Brain* **136**, 1371–1382 (2013).
21. D. X. Medina, M. E. Orr, S. Oddo, Accumulation of C-terminal fragments of transactive response DNA-binding protein 43 leads to synaptic loss and cognitive deficits in human TDP-43 transgenic mice. *Neurobiol. Aging* **35**, 79–87 (2014).
22. W. L. Lin, M. Castanedes-Casey, D. W. Dickson, Transactivation response DNA-binding protein 43 microvasculopathy in frontotemporal degeneration and familial Lewy body disease. *J. Neuropathol. Exp. Neurol.* **68**, 1167–1176 (2009).
23. A. Uchino, H. Takao, H. Hatsuta, Y. Sumikura, Y. Nakano, A. Nogami, Y. Saito, T. Arai, K. Nishiyama, S. Murayama, Incidence and extent of TDP-43 accumulation in aging human brain. *Acta Neuropathol. Commun.* **3**, 35 (2015).
24. R. Takeuchi, Y. Toyoshima, M. Tada, H. Tanaka, H. Shimizu, A. Shiga, T. Miura, K. Aoki, A. Aikawa, S. Ishizawa, T. Ikeuchi, M. Nishizawa, A. Kakita, H. Takahashi, Globular glial mixed four repeat tau and TDP-43 proteinopathy with motor neuron disease and frontotemporal dementia. *Brain Pathol.* **26**, 82–94 (2016).
25. T. Mishima, S. Koga, W. L. Lin, K. Kasanuki, M. Castanedes-Casey, Z. K. Wszolek, S. J. Oh, Y. Tsuboi, D. W. Dickson, Perry syndrome: A distinctive type of TDP-43 proteinopathy. *J. Neuropathol. Exp. Neurol.* **76**, 676–682 (2017).
26. R. C. Paolicelli, A. Jawaid, C. M. Henstridge, A. Valeri, M. Merlini, J. L. Robinson, E. B. Lee, J. Rose, S. Appel, V. M. Lee, J. Q. Trojanowski, T. Spires-Jones, P. E. Schulz, L. Rajendran, TDP-43 depletion in microglia promotes amyloid clearance but also induces synapse loss. *Neuron* **95**, 297–308.e6 (2017).
27. S. Koga, W. L. Lin, R. L. Walton, O. A. Ross, D. W. Dickson, TDP-43 pathology in multiple system atrophy: Colocalization of TDP-43 and α-synuclein in glial cytoplasmic inclusions. *Neuropathol. Appl. Neurobiol.* **44**, 707–721 (2018).
28. K. Weskamp, E. M. Tank, R. Miguez, J. P. McBride, N. B. Gomez, M. White, Z. Lin, C. M. Gonzalez, A. Serio, J. Sreedharan, S. J. Barmada, Shortened TDP43 isoforms upregulated by neuronal hyperactivity drive TDP43 pathology in ALS. *J. Clin. Invest.* **130**, 1139–1155 (2020).
29. D. Ditsworth, M. Maldonado, M. McAlonis-Downes, S. Sun, A. Seelman, K. Drenner, E. Arnold, S. C. Ling, D. Pizzo, J. Ravits, D. W. Cleveland, S. Da Cruz, Mutant TDP-43 within motor neurons drives disease onset but not progression in amyotrophic lateral sclerosis. *Acta Neuropathol.* **133**, 907–922 (2017).
30. J. Tong, C. Huang, F. Bi, Q. Wu, B. Huang, X. Liu, F. Li, H. Zhou, X. G. Xia, Expression of ALS-linked TDP-43 mutant in astrocytes causes non-cell-autonomous motor neuron death in rats. *EMBO J.* **32**, 1917–1926 (2013).
31. A. Y. T. Peng, I. Agrawal, W. Y. Ho, Y. C. Yen, A. J. Pinter, J. Liu, Q. X. C. Phua, K. B. Koh, J. C. Chang, E. Sanford, J. H. K. Man, P. Wong, D. H. Gutmann, S. C. Ling, Loss of TDP-43 in astrocytes leads to motor deficits by triggering A1-like reactive phenotype and triglial dysfunction. *Proc. Natl. Acad. Sci. U.S.A.* **117**, 29101–29112 (2020).
32. D. C. Diaper, Y. Adachi, L. Lazarou, M. Greenstein, F. A. Simoes, A. Di Domenico, D. A. Solomon, S. Lowe, R. Alsubaie, D. Cheng, S. Buckley, D. M. Humphrey, C. E. Shaw, F. Hirth, *Drosophila* TDP-43 dysfunction in glia and muscle cells cause cytological and behavioural phenotypes that characterize ALS and FTLD. *Hum. Mol. Genet.* **22**, 3883–3893 (2013).
33. A. Serio, B. Bilican, S. J. Barmada, D. M. Ando, C. Zhao, R. Siller, K. Burr, G. Haghi, D. Story, A. L. Nishimura, M. A. Carrasco, H. P. Phatnani, C. Shum, I. Wilmut, T. Maniatis, C. E. Shaw, S. Finkbeiner, S. Chandran, Astrocyte pathology and the absence of non-cell autonomy in an induced pluripotent stem cell model of TDP-43 proteinopathy. *Proc. Natl. Acad. Sci. U.S.A.* **110**, 4697–4702 (2013).
34. E. B. Lee, S. Porta, G. M. Baer, Y. Xu, Y. E. Suh, L. K. Kwong, L. Elman, M. Grossman, V. M. Lee, D. J. Irwin, V. M. Van Deerlin, J. Q. Trojanowski, Expansion of the classification of FTLD-TDP: Distinct pathology associated with rapidly progressive frontotemporal degeneration. *Acta Neuropathol.* **134**, 65–78 (2017).
35. W. S. Chung, C. A. Welsh, B. A. Barres, B. Stevens, Do glia drive synaptic and cognitive impairment in disease? *Nat. Neurosci.* **18**, 1539–1545 (2015).

36. M. Pekny, M. Pekna, A. Messing, C. Steinhauser, J. M. Lee, V. Parpura, E. M. Hol, M. V. Sofroniew, A. Verkhratsky, Astrocytes: A central element in neurological diseases. *Acta Neuropathol.* **131**, 323–345 (2016).

37. E. Blanco-Suarez, A. L. Caldwell, N. J. Allen, Role of astrocyte-synapse interactions in CNS disorders. *J. Physiol.* **595**, 1903–1916 (2017).

38. C. Florian, C. G. Vecsey, M. M. Halassa, P. G. Haydon, T. Abel, Astrocyte-derived adenosine and A1 receptor activity contribute to sleep loss-induced deficits in hippocampal synaptic plasticity and memory in mice. *J. Neurosci.* **31**, 6956–6962 (2011).

39. A. G. Orr, E. C. Hsiao, M. M. Wang, K. Ho, D. H. Kim, X. Wang, W. Guo, J. Kang, G. Q. Yu, A. Adame, N. Devidze, D. B. Dubal, E. Masliah, B. R. Conklin, L. Mucke, Astrocytic adenosine receptor A2A and Gs-coupled signaling regulate memory. *Nat. Neurosci.* **18**, 423–434 (2015).

40. S. Sultan, L. Li, J. Moss, F. Petrelli, F. Casse, E. Gebara, J. Lopatar, F. W. Pfrieger, P. Bezzi, J. Bischofberger, N. Toni, Synaptic integration of adult-born hippocampal neurons is locally controlled by astrocytes. *Neuron* **88**, 957–972 (2015).

41. T. Papouin, J. M. Dunphy, M. Tolman, K. T. Dineley, P. G. Haydon, Septal cholinergic neuromodulation tunes the astrocyte-dependent gating of hippocampal NMDA receptors to wakefulness. *Neuron* **94**, 840–854.e7 (2017).

42. A. K. Walker, K. J. Spiller, G. Ge, A. Zheng, Y. Xu, M. Zhou, K. Tripathy, L. K. Kwong, J. Q. Trojanowski, V. M. Lee, Functional recovery in new mouse models of ALS/FTLD after clearance of pathological cytoplasmic TDP-43. *Acta Neuropathol.* **130**, 643–660 (2015).

43. T. Arai, I. R. Mackenzie, M. Hasegawa, T. Nonoka, K. Niizato, K. Tsuchiya, S. Iritani, M. Onaya, H. Akiyama, Phosphorylated TDP-43 in Alzheimer's disease and dementia with Lewy bodies. *Acta Neuropathol.* **117**, 125–136 (2009).

44. H. S. Yang, L. Yu, C. C. White, L. B. Chibnik, J. P. Chhatwal, R. A. Sperling, D. A. Bennett, J. A. Schneider, P. L. De Jager, Evaluation of TDP-43 proteinopathy and hippocampal sclerosis in relation to APOE ε4 haplotype status: A community-based cohort study. *Lancet Neurol.* **17**, 773–781 (2018).

45. R. S. Wilson, J. Yang, L. Yu, S. E. Leurgans, A. W. Capuano, J. A. Schneider, D. A. Bennett, P. A. Boyle, Postmortem neurodegenerative markers and trajectories of decline in cognitive systems. *Neurology* **92**, e831–e840 (2019).

46. C. V. Vorhees, M. T. Williams, Morris water maze: Procedures for assessing spatial and related forms of learning and memory. *Nat. Protoc.* **1**, 848–858 (2006).

47. A. C. Tien, H. H. Tsai, A. V. Molofsky, M. McMahon, L. C. Foo, A. Kaul, J. D. Dougherty, N. Heintz, D. H. Gutmann, B. A. Barres, D. H. Rowitch, Regulated temporal-spatial astrocyte precursor cell proliferation involves BRAF signalling in mammalian spinal cord. *Development* **139**, 2477–2487 (2012).

48. L. C. Foo, J. D. Dougherty, Aldh1L1 is expressed by postnatal neural stem cells in vivo. *Glia* **61**, 1533–1541 (2013).

49. H. Hochgerner, A. Zeisel, P. Lonnerberg, S. Linnarsson, Conserved properties of dentate gyrus neurogenesis across postnatal development revealed by single-cell RNA sequencing. *Nat. Neurosci.* **21**, 290–299 (2018).

50. F. Beyer, W. Ludje, J. Karpf, G. Saher, R. Beckervordersandforth, Distribution of Aldh1L1-CreER^T2 recombination in astrocytes versus neural stem cells in the neurogenic niches of the adult mouse brain. *Front. Neurosci.* **15**, 713077 (2021).

51. Y. Lee, A. Messing, M. Su, M. Brenner, GFAP promoter elements required for region-specific and astrocyte-specific expression. *Glia* **56**, 481–493 (2008).

52. K. Y. Chan, M. J. Jang, B. B. Yoo, A. Greenbaum, N. Ravi, W. L. Wu, L. Sanchez-Guardado, C. Lois, S. K. Mazmanian, B. E. Deverman, V. Gradinaru, Engineered AAVs for efficient noninvasive gene delivery to the central and peripheral nervous systems. *Nat. Neurosci.* **20**, 1172–1179 (2017).

53. Y. F. Xu, T. F. Gendron, Y. J. Zhang, W. L. Lin, S. D'Alton, H. Sheng, M. C. Casey, J. Tong, J. Knight, X. Yu, R. Rademakers, K. Boylan, M. Hutton, E. McGowan, D. W. Dickson, J. Lewis, L. Petrucelli, Wild-type human TDP-43 expression causes TDP-43 phosphorylation, mitochondrial aggregation, motor deficits, and early mortality in transgenic mice. *J. Neurosci.* **30**, 10851–10859 (2010).

54. C. H. Yu, S. Davidson, C. R. Harapas, J. B. Hilton, M. J. Mlodzianoski, P. Laohamonthonkul, C. Louis, R. R. J. Low, J. Moecking, D. De Nardo, K. R. Balka, D. J. Calleja, F. Moghaddas, E. Ni, C. A. McLean, A. L. Samson, S. Tyebji, C. J. Tonkin, C. R. Bye, B. J. Turner, G. Pepin, M. P. Gantier, K. L. Rogers, K. McArthur, P. J. Crouch, S. L. Masters, TDP-43 triggers mitochondrial DNA release via mPTP to activate cGAS/STING in ALS. *Cell* **183**, 636–649.e18 (2020).

55. M. Xie, Y. U. Liu, S. Zhao, L. Zhang, D. B. Bosco, Y. P. Pang, J. Zhong, U. Sheth, Y. A. Martens, N. Zhao, C. C. Liu, Y. Zhuang, L. Wang, D. W. Dickson, M. P. Mattson, G. Bu, L. J. Wu, TREM2 interacts with TDP-43 and mediates microglial neuroprotection against TDP-43-related neurodegeneration. *Nat. Neurosci.* **25**, 26–38 (2022).

56. A. Adamsky, I. Goshen, Astrocytes in memory function: Pioneering findings and future directions. *Neuroscience* **370**, 14–26 (2018).

57. M. Santello, N. Toni, A. Volterra, Astrocyte function from information processing to cognition and cognitive impairment. *Nat. Neurosci.* **22**, 154–166 (2019).

58. V. Swarup, D. Phaneuf, N. Dupre, S. Petri, M. Strong, J. Kriz, J. P. Julien, Deregulation of TDP-43 in amyotrophic lateral sclerosis triggers nuclear factor κB–mediated pathogenic pathways. *J. Exp. Med.* **208**, 2429–2447 (2011).

59. W. Zhao, D. R. Beers, S. Bell, J. Wang, S. Wen, R. H. Baloh, S. H. Appel, TDP-43 activates microglia through NF-κB and NLRP3 inflammasome. *Exp. Neurol.* **273**, 24–35 (2015).

60. Y. Yoshiyama, M. Higuchi, B. Zhang, S. M. Huang, N. Iwata, T. C. Saido, J. Maeda, T. Suhara, J. Q. Trojanowski, V. M.-Y. Lee, Synapse loss and microglial activation precede tangles in a P301S tauopathy mouse model. *Neuron* **53**, 337–351 (2007).

61. A. Litvinchuk, Y. W. Wan, D. B. Swartzlander, F. Chen, A. Cole, N. E. Propson, Q. Wang, B. Zhang, Z. Liu, H. Zheng, Complement C3aR inactivation attenuates tau pathology and reverses an immune network deregulated in tauopathy models and Alzheimer's disease. *Neuron* **100**, 1337–1353.e5 (2018).

62. M. Q. Xia, B. J. Bacskai, R. B. Knowles, S. X. Qin, B. T. Hyman, Expression of the chemokine receptor CXCR3 on neurons and the elevated expression of its ligand IP-10 in reactive astrocytes: In vitro ERK1/2 activation and role in Alzheimer's disease. *J. Neuroimmunol.* **108**, 227–235 (2000).

63. J. R. Groom, J. Richmond, T. T. Murooka, E. W. Sorensen, J. H. Sung, K. Bankert, U. H. von Andrian, J. J. Moon, T. R. Mempel, A. D. Luster, CXCR3 chemokine receptor-ligand interactions in the lymph node optimize CD4+ T helper 1 cell differentiation. *Immunity* **37**, 1091–1103 (2012).

64. F. Sierro, C. Biben, L. Martinez-Munoz, M. Mellado, R. M. Ransohoff, M. Li, B. Woehl, H. Leung, J. Groom, M. Batten, R. P. Harvey, A. C. Martinez, C. R. Mackay, F. Mackay, Disrupted cardiac development but normal hematopoiesis in mice deficient in the second CXCL12/SDF-1 receptor, CXCR7. *Proc. Natl. Acad. Sci. U.S.A.* **104**, 14759–14764 (2007).

65. S. Monteiro, F. M. Ferreira, V. Pinto, S. Roque, M. Morais, D. de Sa-Calcada, C. Mota, M. Correia-Neves, J. J. Cerqueira, Absence of IFNγ promotes hippocampal plasticity and enhances cognitive performance. *Transl. Psychiatry* **6**, e707 (2016).

66. A. J. Filiano, Y. Xu, N. J. Tustison, R. L. Marsh, W. Baker, I. Smirnov, C. C. Overall, S. P. Gadani, S. D. Turner, Z. Weng, S. N. Peerzade, H. Chen, K. S. Lee, M. M. Scott, M. P. Beenhakker, V. Litvak, J. Kipnis, Unexpected role of interferon-γ in regulating neuronal connectivity and social behaviour. *Nature* **535**, 425–429 (2016).

67. S. Monteiro, S. Roque, F. Marques, M. Correia-Neves, J. J. Cerqueira, Brain interference: Revisiting the role of IFNγ in the central nervous system. *Prog. Neurobiol.* **156**, 149–163 (2017).

68. T. Blank, M. Prinz, Type I interferon pathway in CNS homeostasis and neurological disorders. *Glia* **65**, 1397–1406 (2017).

69. I. Broce, C. M. Karch, N. Wen, C. C. Fan, Y. Wang, C. H. Tan, N. Kouri, O. A. Ross, G. U. Hoglinger, U. Muller, J. Hardy; International FTD-Genomics Consortium, P. Momeni, C. P. Hess, W. P. Dillon, Z. A. Miller, L. W. Bonham, G. D. Rabinovici, H. J. Rosen, G. D. Schellenberg, A. Franke, T. H. Karlsen, J. H. Veldink, R. Ferrari, L. P. Sugrue, B. L. Miller, O. A. Andreassen, A. M. Dale, R. S. Desikan, Immune-related genetic enrichment in frontotemporal dementia: An analysis of genome-wide association studies. *PLOS Med.* **15**, e1002487 (2018).

70. M. J. Gandal, P. Zhang, E. Hadjimichael, R. L. Walker, C. Chen, S. Liu, H. Won, H. van Bakel, M. Varghese, Y. Wang, A. W. Shieh, S. Haney, S. Parhami, J. Belmont, M. Kim, P. Moran Losada, Z. Khan, J. Mleczko, Y. Xia, R. Dai, D. Wang, Y. T. Yang, M. Xu, K. Fish, P. R. Hof, J. Warrell, D. Fitzgerald, K. White, A. E. Jaffe; PsychENCODE Consortium, M. A. Peters, M. Gerstein, C. Liu, L. M. Iakoucheva, D. Pinto, D. H. Geschwind, Transcriptome-wide isoform-level dysregulation in ASD, schizophrenia, and bipolar disorder. *Science* **362**, eaat8127 (2018).

71. S. Lee, S. Kim, H. Y. Kang, H. R. Lim, Y. Kwon, M. Jo, Y. M. Jeon, S. R. Kim, K. Kim, C. M. Ha, S. Lee, H. J. Kim, The overexpression of TDP-43 in astrocytes causes neurodegeneration via a PTP1B-mediated inflammatory response. *J. Neuroinflammation* **17**, 299 (2020).

72. K. Dutta, S. S. Thammisetty, C. Boutej, C. Bareil, J. P. Julien, Mitigation of ALS pathology by neuron-specific inhibition of nuclear factor kappa B signaling. *J. Neurosci.* **40**, 5137–5154 (2020).

73. Y. Z. Lin, S. Y. Yao, R. A. Veach, T. R. Torgerson, J. Hawiger, Inhibition of nuclear translocation of transcription factor NF-κB by a synthetic peptide containing a cell membrane-permeable motif and nuclear localization sequence. *J. Biol. Chem.* **270**, 14255–14258 (1995).

74. J. Schust, B. Sperl, A. Hollis, T. U. Mayer, T. Berg, Stattic: A small-molecule inhibitor of STAT3 activation and dimerization. *Chem. Biol.* **13**, 1235–1242 (2006).

75. J. De Miranda, K. Yaddanapudi, M. Hornig, W. I. Lipkin, Astrocytes recognize intracellular polyinosinic-polycytidylic acid via MDA-5. *FASEB J.* **23**, 1064–1071 (2009).

76. R. F. Itzhaki, Herpes simplex virus type 1 and Alzheimer's disease: Increasing evidence for a major role of the virus. *Front. Aging. Neurosci.* **6**, 202 (2014).

77. W. A. Eimer, D. K. Vijaya Kumar, N. K. Navalpur Shanmugam, A. S. Rodriguez, T. Mitchell, K. J. Washicosky, B. Gyorgy, X. O. Breakefield, R. E. Tanzi, R. D. Moir, Alzheimer's disease–associated β-amyloid is rapidly seeded by herpesviridae to protect against brain infection. *Neuron* **99**, 56–63.e3 (2018).

78. J. Velebit, A. Horvat, T. Smolic, S. Prpar Mihevc, B. Rogelj, R. Zorec, N. Vardjan, Astrocytes with TDP-43 inclusions exhibit reduced noradrenergic cAMP and Ca²⁺ signaling and dysregulated cell metabolism. *Sci. Rep.* **10**, 6003 (2020).

79. M. Loetscher, B. Gerber, P. Loetscher, S. A. Jones, L. Piali, I. Clark-Lewis, M. Baggiolini, B. Moser, Chemokine receptor specific for IP10 and mig: Structure, function, and expression in activated T-lymphocytes. *J. Exp. Med.* **184**, 963–969 (1996).

80. K. Biber, I. Dijkstra, C. Trebst, C. J. De Groot, R. M. Ransohoff, H. W. Boddeke, Functional expression of CXCR3 in cultured mouse and human astrocytes and microglia. *Neuroscience* **112**, 487–497 (2002).

81. D. Galimberti, R. Bonsi, C. Fenoglio, M. Serpente, S. M. Cioffi, G. Fumagalli, A. Arighi, L. Ghezzi, M. Arcaro, M. Mercurio, E. Rotondo, E. Scarpini, Inflammatory molecules in frontotemporal dementia: Cerebrospinal fluid signature of progranulin mutation carriers. *Brain Behav. Immun.* **49**, 182–187 (2015).

82. B. K. Atwood, D. M. Lovinger, B. N. Mathur, Presynaptic long-term depression mediated by G$_{i/o}$-coupled receptors. *Trends Neurosci.* **37**, 663–673 (2014).

83. Z. Zurawski, Y. Y. Yim, S. Alford, H. E. Hamm, The expanding roles and mechanisms of G protein-mediated presynaptic inhibition. *J. Biol. Chem.* **294**, 1661–1670 (2019).

84. T. J. Stachniak, A. Ghosh, S. M. Sternson, Chemogenetic synaptic silencing of neural circuits localizes a hypothalamus→midbrain pathway for feeding behavior. *Neuron* **82**, 797–808 (2014).

85. C. Chen, I. Arai, R. Satterfield, S. M. Young Jr., P. Jonas, Synaptotagmin 2 is the fast Ca²⁺ sensor at a central inhibitory synapse. *Cell Rep.* **18**, 723–736 (2017).

86. X. Tong, Y. Ao, G. C. Faas, S. E. Nwaobi, J. Xu, M. D. Haustein, M. A. Anderson, I. Mody, M. L. Olsen, M. V. Sofroniew, B. S. Khakh, Astrocyte Kir4.1 ion channel deficits contribute to neuronal dysfunction in Huntington's disease model mice. *Nat. Neurosci.* **17**, 694–703 (2014).

87. Z. Liu, M. Chopp, Astrocytes, therapeutic targets for neuroprotection and neurorestoration in ischemic stroke. *Prog. Neurobiol.* **144**, 103–120 (2016).

88. B. De Strooper, E. Karran, The cellular phase of Alzheimer's disease. *Cell* **164**, 603–615 (2016).

89. M. S. Windrem, M. Osipovitch, Z. Liu, J. Bates, D. Chandler-Militello, L. Zou, J. Munir, S. Schanz, K. McCoy, R. H. Miller, S. Wang, M. Nedergaard, R. L. Findling, P. J. Tesar, S. A. Goldman, Human iPSC glial mouse chimeras reveal glial contributions to schizophrenia. *Cell Stem Cell* **21**, 195–208.e6 (2017).

90. B. S. Khakh, M. V. Sofroniew, Diversity of astrocyte functions and phenotypes in neural circuits. *Nat. Neurosci.* **18**, 942–952 (2015).

91. L. Ben Haim, D. H. Rowitch, Functional diversity of astrocytes in neural circuit regulation. *Nat. Rev. Neurosci.* **18**, 31–41 (2017).

92. S. Habbas, M. Santello, D. Becker, H. Stubbe, G. Zappia, N. Liaudet, F. R. Klaus, G. Kollias, A. Fontana, C. R. Pryce, T. Suter, A. Volterra, Neuroinflammatory TNFα impairs memory via astrocyte signaling. *Cell* **163**, 1730–1741 (2015).

93. Y. H. Gong, A. S. Parsadanian, A. Andreeva, W. D. Snider, J. L. Elliott, Restricted expression of G86R Cu/Zn superoxide dismutase in astrocytes results in astrocytosis but does not cause motoneuron degeneration. *J. Neurosci.* **20**, 660–665 (2000).

94. M. Nagai, D. B. Re, T. Nagata, A. Chalazonitis, T. M. Jessell, H. Wichterle, S. Przedborski, Astrocytes expressing ALS-linked mutated SOD1 release factors selectively toxic to motor neurons. *Nat. Neurosci.* **10**, 615–622 (2007).

95. K. Yamanaka, S. J. Chun, S. Boillee, N. Fujimori-Tonou, H. Yamashita, D. H. Gutmann, R. Takahashi, H. Misawa, D. W. Cleveland, Astrocytes as determinants of disease progression in inherited amyotrophic lateral sclerosis. *Nat. Neurosci.* **11**, 251–253 (2008).

96. K. Richetin, P. Steullet, M. Pachoud, R. Perbet, E. Parietti, M. Maheswaran, S. Eddarkaoui, S. Begard, C. Pythoud, M. Rey, R. Caillierez, K. Q. Do, S. Halliez, P. Bezzi, L. Buee, G. Leuba, M. Colin, N. Toni, N. Deglon, Tau accumulation in astrocytes of the dentate gyrus induces neuronal dysfunction and memory deficits in Alzheimer's disease. *Nat. Neurosci.* **23**, 1567–1579 (2020).

97. Y. Wu, W. Shao, T. W. Todd, J. Tong, M. Yue, S. Koga, M. Castanedes-Casey, A. L. Librero, C. W. Lee, I. R. Mackenzie, D. W. Dickson, Y. J. Zhang, L. Petrucelli, M. Prudencio, Microglial lysosome dysfunction contributes to white matter pathology and TDP-43 proteinopathy in GRN-associated FTD. *Cell Rep.* **36**, 109581 (2021).

98. T. K. Saldi, P. E. Ash, G. Wilson, P. Gonzales, A. Garrido-Lecca, C. M. Roberts, V. Dostal, T. F. Gendron, L. D. Stein, T. Blumenthal, L. Petrucelli, C. D. Link, TDP-1, the *Caenorhabditis elegans* ortholog of TDP-43, limits the accumulation of double-stranded RNA. *EMBO J.* **33**, 2947–2966 (2014).

99. W. Dunker, X. Ye, Y. Zhao, L. Liu, A. Richardson, J. Karijolich, TDP-43 prevents endogenous RNAs from triggering a lethal RIG-I-dependent interferon response. *Cell Rep.* **35**, 108976 (2021).

100. A. J. Lee, A. A. Ashkar, The dual nature of type I and type II interferons. *Front. Immunol.* **9**, 2061 (2018).

101. E. Y. Liu, J. Russ, C. P. Cali, J. M. Phan, A. Amlie-Wolf, E. B. Lee, Loss of nuclear TDP-43 is associated with decondensation of LINE retrotransposons. *Cell Rep.* **27**, 1409–1421.e6 (2019).

102. Y. H. Chang, J. Dubnau, The gypsy endogenous retrovirus drives non-cell-autonomous propagation in a *Drosophila* TDP-43 model of neurodegeneration. *Curr. Biol.* **29**, 3135–3152.e4 (2019).

103. M. A. Wozniak, A. P. Mee, R. F. Itzhaki, Herpes simplex virus type 1 DNA is located within Alzheimer's disease amyloid plaques. *J. Pathol.* **217**, 131–138 (2009).

104. B. Readhead, J. V. Haure-Mirande, C. C. Funk, M. A. Richards, P. Shannon, V. Haroutunian, M. Sano, W. S. Liang, N. D. Beckmann, N. D. Price, E. M. Reiman, E. E. Schadt, M. E. Ehrlich, S. Gandy, J. T. Dudley, Multiscale analysis of independent Alzheimer's cohorts finds disruption of molecular, genetic, and clinical networks by human herpesvirus. *Neuron* **99**, 64–82.e7 (2018).

105. M. A. Allnutt, K. Johnson, D. A. Bennett, S. M. Connor, J. C. Troncoso, O. Pletnikova, M. S. Albert, S. M. Resnick, S. W. Scholz, P. L. De Jager, S. Jacobson, Human herpesvirus 6 detection in Alzheimer's disease cases and controls across multiple cohorts. *Neuron* **105**, 1027–1035.e2 (2020).

106. J. S. Yokoyama, C. M. Karch, C. C. Fan, L. W. Bonham, N. Kouri, O. A. Ross, R. Rademakers, J. Kim, Y. Wang, G. U. Hoglinger, U. Muller, R. Ferrari, J. Hardy; International FTD-Genomics Consortium (IFGC), P. Momeni, L. P. Sugrue, C. P. Hess, A. J. Barkovich, A. L. Boxer, W. W. Seeley, G. D. Rabinovici, H. J. Rosen, B. L. Miller, N. J. Schmansky, B. Fischl, B. T. Hyman, D. W. Dickson, G. D. Schellenberg, O. A. Andreassen, A. M. Dale, R. S. Desikan, Shared genetic risk between corticobasal degeneration, progressive supranuclear palsy, and frontotemporal dementia. *Acta Neuropathol.* **133**, 825–837 (2017).

107. C. Pottier, Y. Ren, R. B. Perkerson III, M. Baker, G. D. Jenkins, M. van Blitterswijk, M. DeJesus-Hernandez, J. G. J. van Rooij, M. E. Murray, E. Christopher, S. K. McDonnell, Z. Fogarty, A. Batzler, S. Tian, C. T. Vicente, B. Matchett, A. M. Karydas, G. R. Hsiung, H. Seelaar, M. O. Mol, E. C. Finger, C. Graff, L. Oijerstedt, M. Neumann, P. Heutink, M. Synofzik, C. Wilke, J. Prudlo, P. Rizzu, J. Simon-Sanchez, D. Edbauer, S. Roeber, J. Diehl-Schmid, B. M. Evers, A. King, M. M. Mesulam, S. Weintraub, C. Geula, K. F. Bieniek, L. Petrucelli, G. L. Ahern, E. M. Reiman, B. K. Woodruff, R. J. Caselli, E. D. Huey, M. R. Farlow, J. Grafman, S. Mead, L. T. Grinberg, S. Spina, M. Grossman, D. J. Irwin, E. B. Lee, E. Suh, J. Snowden, D. Mann, N. Ertekin-Taner, R. J. Uitti, Z. K. Wszolek, K. A. Josephs, J. E. Parisi, D. S. Knopman, R. C. Petersen, J. R. Hodges, O. Piguet, E. G. Geier, J. S. Yokoyama, R. A. Rissman, E. Rogaeva, J. Keith, L. Zinman, M. C. Tartaglia, N. J. Cairns, C. Cruchaga, B. Ghetti, J. Kofler, O. L. Lopez, T. G. Beach, T. Arzberger, J. Herms, L. S. Honig, J. P. Vonsattel, G. M. Halliday, J. B. Kwok, C. L. White 3rd, M. Gearing, J. Glass, S. Rollinson, S. Pickering-Brown, J. D. Rohrer, J. Q. Trojanowski, V. Van Deerlin, E. H. Bigio, C. Troakes, S. Al-Sarraj, Y. Asmann, B. L. Miller, N. R. Graff-Radford, B. F. Boeve, W. W. Seeley, I. R. A. Mackenzie, J. C. van Swieten, D. W. Dickson, J. M. Biernacka, R. Rademakers, Genome-wide analyses as part of the international FTLD-TDP whole-genome sequencing consortium reveals novel disease risk factors and increases support for immune dysfunction in FTLD. *Acta Neuropathol.* **137**, 879–899 (2019).

108. E. R. Roy, B. Wang, Y. W. Wan, G. Chiu, A. Cole, Z. Yin, N. E. Propson, Y. Xu, J. L. Jankowsky, Z. Liu, V. M. Lee, J. Q. Trojanowski, S. D. Ginsberg, O. Butovsky, H. Zheng, W. Cao, Type I interferon response drives neuroinflammation and synapse loss in Alzheimer disease. *J. Clin. Invest.* **130**, 1912–1930 (2020).

109. S. Hosseini, K. Michaelsen-Preusse, G. Grigoryan, C. Chhatbar, U. Kalinke, M. Korte, Type I interferon receptor signaling in astrocytes regulates hippocampal synaptic plasticity and cognitive function of the healthy CNS. *Cell Rep.* **31**, 107666 (2020).

110. H. Li, Z. Gang, H. Yuling, X. Luokun, X. Jie, L. Hao, W. Li, H. Chunsong, J. Junyan, J. Mingshen, J. Youxin, G. Feili, J. Boquan, T. Jinquan, Different neurotropic pathogens elicit neurotoxic CCR9- or neurosupportive CXCR3-expressing microglia. *J. Immunol.* **177**, 3644–3656 (2006).

111. E. H. Wilson, W. Weninger, C. A. Hunter, Trafficking of immune cells in the central nervous system. *J. Clin. Invest.* **120**, 1368–1379 (2010).

112. C. Patzke, M. M. Brockmann, J. Dai, K. J. Gan, M. K. Grauel, P. Fenske, Y. Liu, C. Acuna, C. Rosenmund, T. C. Südhof, Neuromodulator signaling bidirectionally controls vesicle numbers in human synapses. *Cell* **179**, 498–513.e22 (2019).

113. D. Galimberti, N. Schoonenboom, P. Scheltens, C. Fenoglio, F. Bouwman, E. Venturelli, I. Guidi, M. A. Blankenstein, N. Bresolin, E. Scarpini, Intrathecal chemokine synthesis in mild cognitive impairment and Alzheimer disease. *Arch. Neurol.* **63**, 538–543 (2006).

114. J. J. Palop, L. Mucke, Network abnormalities and interneuron dysfunction in Alzheimer disease. *Nat. Rev. Neurosci.* **17**, 777–792 (2016).

115. M. Krauthausen, M. P. Kummer, J. Zimmermann, E. Reyes-Irisarri, D. Terwel, B. Bulic, M. T. Heneka, M. Muller, CXCR3 promotes plaque formation and behavioral deficits in an Alzheimer's disease model. *J. Clin. Invest.* **125**, 365–378 (2015).

116. S. P. Andrews, R. J. Cox, Small molecule CXCR3 antagonists. *J. Med. Chem.* **59**, 2894–2917 (2016).

117. A. C. Elden, H. J. Kim, M. P. Hart, A. S. Chen-Plotkin, B. S. Johnson, X. Fang, M. Armakola, F. Geser, R. Greene, M. M. Lu, A. Padmanabhan, D. Clay-Falcone, L. McCluskey, L. Elman, D. Juhr, P. J. Gruber, U. Rüb, G. Auburger, J. Q. Trojanowski, V. M. Lee, V. M.-Y. Van Deerlin, N. M. Bonini, A. D. Gitler, Ataxin-2 intermediate-length polyglutamine expansions are associated with increased risk for ALS. *Nature* **466**, 1069–1075 (2010).

118. P. Sharma, D. M. Ando, A. Daub, J. A. Kaye, S. Finkbeiner, High-throughput screening in primary neurons. *Methods Enzymol.* **506**, 331–360 (2012).

119. S. Bolte, F. P. Cordelieres, A guided tour into subcellular colocalization analysis in light microscopy. *J. Microsc.* **224**, 213–232 (2006).

120. S. A. Liddelow, K. A. Guttenplan, L. E. Clarke, F. C. Bennett, C. J. Bohlen, L. Schirmer, M. L. Bennett, A. E. Munch, W. S. Chung, T. C. Peterson, D. K. Wilton, A. Frouin, B. A. Napier, N. Panicker, M. Kumar, M. S. Buckwalter, D. H. Rowitch, V. L. Dawson, T. M. Dawson, B. Stevens, B. A. Barres, Neurotoxic reactive astrocytes are induced by activated microglia. *Nature* **541**, 481–487 (2017).